PAPER

Ba-filled Ni–Sb–Sn based skutterudites with anomalously high lattice thermal conductivity†‡

W. Paschinger,*[a] G. Rogl,[a,b,c,d] A. Grytsiv,[a,b,c] H. Michor,[c] P. R. Heinrich,[c] H. Müller,[c] S. Puchegger,[d] B. Klobes,§[e] R. P. Hermann,[e,f] M. Reinecker,[d] Ch. Eisenmenger-Sitter,[c] P. Broz,[g] E. Bauer,[b,c] G. Giester,[h] M. Zehetbauer[d] and P. F. Rogl[a,b]

Novel filled skutterudites $Ba_yNi_4Sb_{12-x}Sn_x$ (y_{max} = 0.93) have been prepared by arc melting followed by annealing at 250, 350 and 450 °C up to 30 days in vacuum-sealed quartz vials. Extension of the homogeneity region, solidus temperatures and structural investigations were performed for the skutterudite phase in the ternary Ni–Sn–Sb and in the quaternary Ba–Ni–Sb–Sn systems. Phase equilibria in the Ni–Sn–Sb system at 450 °C were established by means of Electron Probe Microanalysis (EPMA) and X-ray Powder Diffraction (XPD). With rather small cages $Ni_4(Sb,Sn)_{12}$, the Ba–Ni–Sn–Sb skutterudite system is perfectly suited to study the influence of filler atoms on the phonon thermal conductivity. Single-phase samples with the composition $Ni_4Sb_{8.2}Sn_{3.8}$, $Ba_{0.42}Ni_4Sb_{8.2}Sn_{3.8}$ and $Ba_{0.92}Ni_4Sb_{6.7}Sn_{5.3}$ were used to measure their physical properties, *i.e.* temperature dependent electrical resistivity, Seebeck coefficient and thermal conductivity. The resistivity data demonstrate a crossover from metallic to semiconducting behaviour. The corresponding gap width was extracted from the maxima in the Seebeck coefficient data as a function of temperature. Single crystal X-ray structure analyses at 100, 200 and 300 K revealed the thermal expansion coefficients as well as Einstein and Debye temperatures for $Ba_{0.73}Ni_4Sb_{8.1}Sn_{3.9}$ and $Ba_{0.95}Ni_4Sb_{6.1}Sn_{5.9}$. These data were in accordance with the Debye temperatures obtained from the specific heat (4.4 K < T < 140 K) and Mössbauer spectroscopy (10 K < T < 290 K). Rather small atom displacement parameters for the Ba filler atoms indicate a severe reduction in the "rattling behaviour" consistent with the high levels of lattice thermal conductivity. The elastic moduli, collected from Resonant Ultrasonic Spectroscopy ranged from 100 GPa for $Ni_4Sb_{8.2}Sn_{3.8}$ to 116 GPa for $Ba_{0.92}Ni_4Sb_{6.7}Sn_{5.3}$. The thermal expansion coefficients were 11.8×10^{-6} K^{-1} for $Ni_4Sb_{8.2}Sn_{3.8}$ and 13.8×10^{-6} K^{-1} for $Ba_{0.92}Ni_4Sb_{6.7}Sn_{5.3}$. The room temperature Vickers hardness values vary within the range from 2.6 GPa to 4.7 GPa. Severe plastic deformation *via* high-pressure torsion was used to introduce nanostructuring; however, the physical properties before and after HPT showed no significant effect on the materials thermoelectric behaviour.

[a]*Institute of Materials Chemistry & Research, University of Vienna, Währinger Straße 42, A-1090 Vienna, Austria. E-mail: werner.paschinger@univie.ac.at*
[b]*Christian Doppler Laboratory for Thermoelectricity, Vienna, Austria*
[c]*Institute for Solid State Physics, TU-Wien, Wiedner Hauptstr. 8, A-1040 Vienna, Austria*
[d]*Faculty of Physics, University of Vienna, Boltzmanngasse 5, A-1090 Vienna, Austria*
[e]*Jülich Centre for Neutron Science JCNS and Peter Grünberg Institute PGI, JARA-FIT, Forschungszentrum Jülich GmbH, D-52425 Jülich, Germany*
[f]*Materials Science and Technology Division, Oak Ridge National Laboratory, Oak Ridge, Tennessee 37831, USA*
[g]*Faculty of Science, Deparment of Chemistry, Masaryk University, Kotlářská 267/2, 611 37 Brno, Czech Republic*
[h]*Institute of Mineralogy and Crystallography, University of Vienna, Althanstr. 14 (UZA 2), A-1090 Vienna, Austria*
†In Memoriam of Dr John F. "Jack" Smith.
‡Electronic supplementary information (ESI) available. See DOI: 10.1039/c6dt01298a
§Present address: Gesellschaft für Anlagen- und Reaktionssicherheit (GRS) gGmbH, Schwertnergasse 1, 50667 Köln, Germany.

1. Introduction

Several classes of thermoelectric materials have been investigated for renewable power generation applications, including tellurides,[1,2] half-Heuslers,[3,4] silicides[5] and skutterudites. Skutterudite-based materials have attracted considerable research interest since a long time[6] because they show a large variety of physical properties. However, for commercial thermoelectric applications,[7] high figures of merit

$$zT = \frac{S^2 \cdot T}{\rho \cdot \kappa} \quad (1.1)$$

for the p-type as well as for n-type configuration are a precondition.[8–11] Skutterudites crystallize in the cubic $CoAs_3$ structure (space group $Im\bar{3}$) with the general formula $F_xT_4M_{12}$,

where T is a transition metal of the VIIIth group located in position 8c $(\frac{1}{4}, \frac{1}{4}, \frac{1}{4})$ and M is a pnictogen, chalcogen or an element of the IVth main-group in the Wyckoff site 24g $(0, y, z)$. These atoms form a cage-like structure with a large icosahedral void at the 2a site $(0, 0, 0)$, which may accommodate various filler atoms F, including alkaline and alkaline earth metals, lanthanoids, actinoids, as well as halogens or in particular cases Y, Hf,[12,13] Pb and Sn.[14–17] A ternary skutterudite in the system Ni–Sn–Sb was first reported by Grytsiv et al.[18] who defined a wide homogeneity range at 250 °C and 350 °C by establishing the isothermal sections in the Sn–Sb–NiSb–Ni$_3$Sn$_2$ subsystem at these temperatures. Investigations by Mishra et al.[19] in the Sn-rich part of the Ni–Sn–Sb phase diagram suggested that the phase equilibria determined by Grytsiv et al.[18] lies within 10 °C above or below the declared temperatures.

Numerous reports (see for example ref. 18, 20–25) describe mixed occupancies for all three crystallographic sites (24g, 8c, 2a). For Ni–Sn–Sb based skutterudites, the structure with Ni-atoms fully occupying the 8c site seems to be stabilized by a random distribution of Sb and Sn atoms in the 24g position because in the binary systems, Ni-{Sn, P, As, Sb}, only the skutterudite NiP$_3$ exists as a high temperature modification.[26,27] A special situation occurs for Sn-atoms, which may occupy the 24g site, but may simultaneously enter the 2a site of the same compound reaching filling levels of 0.21 in this position.[18] Ternary and isotypic quaternary skutterudites with Eu and Yb as filler elements have been characterised by their physical properties as well as by Raman and Mössbauer spectroscopy, unambiguously revealing that a small amount of Sn is able to enter the 2a $(0, 0, 0)$ site.[18] The filler atom in 2a in most skutterudites is loosely bound in the large icosahedral cage and is generally believed to decrease the thermal conductivity of the material via rattling modes.[6,28] With Ni and Sn atoms being smaller than Fe, Co and Sb, respectively, the Ni$_4$(Sn,Sb)$_{12}$ icosahedral cages are smaller in comparison to a large filler atom such as Ba (for details see section 5: the crystal structure and vibration modes of Ba$_y$Ni$_4$Sb$_{12-x}$Sn$_x$). Thus, the Ba–Ni–Sn–Sb skutterudite system may become a model system to study the influence of filler atoms on the phonon thermal conductivity.

In addition, not much information is available on the thermal stability of Ni-skutterudites. To the best of our knowledge, the melting temperatures were determined for only two binary skutterudites, CoAs$_3$[29] and CoSb$_3$,[30] and there are no data either on the influence of the filler on the melting points or on the thermal stability of ternary or multi-component skutterudites.

The current article will focus on a series of aspects outlined below:

(i) The Ni–Sn–Sb isothermal section at 450 °C and the extension of the ternary skutterudite phase Ni$_4$Sb$_{12-x}$Sn$_x$ in comparison with data reported by Grytsiv et al.[18]

(ii) The temperature dependent filling levels of Ba$_y$Ni$_4$Sb$_{12-x}$Sn$_x$.

(iii) The solidus surface for the ternary and quaternary skutterudites, Ni$_4$Sb$_{12-x}$Sn$_x$ and Ba$_y$Ni$_4$Sb$_{12-x}$Sn$_x$, in dependence of their composition.

(iv) The structure of Ba$_y$Ni$_4$Sb$_{12-x}$Sn$_x$ determined by single crystal X-ray diffraction.

(v) Physical property measurements such as temperature dependent resistivities, thermal conductivities and Seebeck coefficients of three single-phase samples: Ni$_4$Sb$_{8.2}$Sn$_{3.8}$, Ba$_{0.42}$Ni$_4$Sb$_{8.24}$Sn$_{3.8}$ and Ba$_{0.92}$Ni$_4$Sb$_{6.7}$Sn$_{5.3}$.

(vi) The effect of Severe Plastic Deformation (SPD) via High-Pressure Torsion on the material.

(vii) Mechanical properties such as thermal expansion, elastic moduli and Vicker's hardness of Ni$_4$Sb$_{8.2}$Sn$_{3.8}$, Ba$_{0.42}$Ni$_4$Sb$_{8.3}$Sn$_{3.8}$ and Ba$_{0.92}$Ni$_4$Sb$_{6.7}$Sn$_{5.3}$.

(viii) A discussion on the thermoelectric behaviour in terms of the electron and phonon mean free paths and the influence of Ba-filler level on the lattice thermal conductivity.

2. Experimental

Sample preparation

Starting materials were used in the form of elemental pieces of Ba, Ni, Sb and Sn, all of 99.95 mass% minimum purity. Samples suitable for constitutional analysis were prepared by one of the following optimised melting reactions directly gaining the ternary Ni$_4$Sb$_x$Sn$_{12-x}$ alloys, whereas for the quaternary skutterudites, the filler element was added in a second reaction step:

(i) Bulk alloys, each with a total weight of 1–2 g, were synthesized via a Ni$_4$Sb$_x$Sn$_{12-x}$ master alloy by argon arc melting of metal ingots on a water-cooled copper hearth, adding the filler element to the ternary alloy using the same reaction method.

(ii) Samples with the nominal composition Ni$_4$Sb$_x$Sn$_{12-x}$ (1–2 g) were prepared from stoichiometric amounts of high purity Sb and Sn pieces and fine Ni wire. After mixing, the material was sealed into evacuated quartz tubes, heated to 980 °C, kept in the liquid state for half an hour prior to quenching the capsules in air. For the quaternary samples, the whole procedure was repeated, adding pieces of Ba to the ternary master alloys. Total weight losses of 1–3 mass% that occurred during sample preparation were attributed to the high vapour pressures of Sb and Ba and were compensated by adding an additional 3–5 mass% of Ba and Sb. All the samples were then sealed in evacuated quartz tubes, annealed at 250, 350 or 450 °C for 3 to 30 days for equilibration before quenching in cold water.

Large single-phase samples (6–8 g) in cylindrical form for the study of their physical properties were prepared following either route (i) or (ii); the specimens were further ground to a grain size below at least 100 μm inside an Argon glove box using a WC mortar followed by ball-milling in a Fritsch planetary mill (Pulverisette 4) with WC-balls of 1.6 mm, rotation speed 250 and ratio of −2.5 for 2 h to gain a nanocrystalline powder. These powders were then loaded into 1 cm diameter graphite cartridges for hot-pressing under 1 bar of 5N-argon in a FTC uniaxial hotpress system (HP W 200/250 2200-200-KS).

The Sb-rich specimens, $Ni_4Sb_{8.2}Sn_{3.8}$ and $Ba_{0.42}Ni_4Sb_{8.2}Sn_{3.8}$, were directly prepared by hot pressing at 450 °C, resulting in a densely compacted single-phase material.

For the Sn-rich sample, $Ba_{0.92}Ni_4Sb_{6.7}Sn_{5.3}$, a modified preparation method had to be chosen. 5–10 mass% of extra Sb and Sn were added from the very beginning of the synthesis. The ball-milled powder was pre-compacted and annealed under argon at 450 °C overnight inside the hotpress, followed by hotpressing at 430 °C in order to squeeze out the surplus Sb_2Sn_3.

Small single crystals suitable for temperature dependent X-ray structure analysis were obtained from flux techniques: Sn-rich single crystals of $Ba_{0.95}Ni_4Sb_{6.1}Sn_{5.9}$ were prepared from Sn flux, Sb-rich $Ba_{0.73}Ni_4Sb_{8.1}Sn_{3.9}$ single crystals from Sb_2Sn_3 flux by heating the starting materials with compositions 2Ba–12Ni–Sb22.5–Sn63.5 and 2Ba–8Ni–45Sb–45Sn, respectively, to 950 °C to reach the liquid state followed by cooling at a rate of 12 °C h^{-1} to 450 °C. The alloys were maintained at this temperature for 3 days to reach thermodynamic equilibrium. Subsequently, the samples were removed from the furnace and the Sn-rich sample was treated with hot concentrated HCl acid to dissolve the Sn-rich matrix. For the Sb-rich single crystals, the Sb_2Sn_3-rich matrix was removed using hot concentrated HNO_3 and then the crystals were washed with cold concentrated HCl.

Sample characterisation

X-ray powder diffraction (XPD) data were collected using a Huber Guinier camera with monochromatic Cu $K_{\alpha 1}$ radiation ($\lambda = 0.154056$ nm) and an image plate recording system (model G670). Pure Si ($a_{Si} = 0.5431065$ nm) was used as internal standard to determine the precise lattice parameters *via* least-squares fitting to the indexed 2θ values employing the program STRUKTUR.[31] For quantitative Rietveld refinements, we applied the program FULLPROF.[32] The chemical compositions of the different specimens were extracted from electron probe microanalyses (EPMA) using energy-dispersive X-ray (EDX) spectroscopy with an INCA Penta FETx3-Zeiss SUPRA55VP equipment (Oxford Instruments).

After inspection on an AXS-GADDS texture goniometer for quality and crystal symmetry, the X-ray intensity data for the two single crystals were collected on a four-circle Nonius Kappa diffractometer with a charge-coupled device (CCD) area detector and graphite-monochromated Mo K_α radiation ($\lambda = 0.07107$ nm) at 100, 200 and 300 K under nitrogen gas. The orientation matrix and unit cell parameters were derived using the program DENZO.[33] In addition to the general treatment of absorption effects using the multi-scan technique (SADABS; redundancy of integrated reflections >8), no individual absorption correction was necessary because of the regular shape and small dimensions of the crystals. Employing SHELXS-97 and SHELXL-97 software[34] for the single-crystal X-ray diffraction data, the structures were successfully solved using direct methods and refined.

Using Archimedes' principle and distilled water, the density ρ_s of the hot pressed samples was determined and compared to the calculated X-ray densities.

$$\rho_X = \frac{Z \cdot M}{N \cdot V} \qquad (2.1)$$

where M is the molar mass, Z is the number of formula units per cell, N is Avogadro's number and V is the volume of the unit cell.

Mössbauer spectroscopy

Mössbauer spectra were obtained on a constant-acceleration spectrometer using a 300 µCi $Ca^{121}SbO_3$ source and a 10 mCi $Ca^{119m}SnO_3$ source for ^{121}Sb- and ^{119}Sn-Mössbauer spectroscopy, respectively. The velocity was calibrated with α-Fe at room temperature utilizing a $^{57}Co/Rh$ source. All Mössbauer spectra were obtained using powder samples and the isomer shifts are with reference to InSb at 10 K and to $CaSnO_3$ at room temperature. The significant γ-background due to the fluorescence of the source for ^{119}Sn-Mössbauer spectroscopy was suppressed with a 50 µm Pd foil between the source and detector.

Physical property measurements

The electrical resistivity, Seebeck coefficient and thermal conductivity were measured (4 K < T < 300 K) using a homemade equipment cooled by liquid He (see ref. 35). The Seebeck coefficient and electrical resistivity above room temperature were measured simultaneously with a ULVAC-ZEM 3 (Riko, Japan) apparatus. The thermal diffusivity D_t was measured using a flash method (Flashline-3000, ANTER, USA). The thermal conductivity κ was calculated from D_t, the specific heat C_p and the density ρ_s employing the relationship $\kappa = D_t \cdot C_p \cdot \rho_s$. Hall data were obtained by a Quantum Design physical properties measurement system (PPMS) using a standard six-point method in a magnetic field of 9 T. Specific heat measurements from 2 to 140 K were performed on single-phase samples with masses between 2.5 g and 5 g cooled with liquid He employing an adiabatic step heating technique.

Thermal expansion measurements

The thermal expansion from 4.2 K to 300 K was measured with a miniature capacitance dilatometer[36] using the tilted plate principle.[37,38] For this measurement, the sample was placed in a hole of the lower ring-like silver capacitance plate, which is separated from the silver upper capacitor plate by two needle bearings. For measurement of the thermal expansion between 80 and 420 K, a dynamic mechanical analyzer DMA7 (Perkin Elmer Inc.) was employed. The sample was positioned in a parallel plate mode with a quartz rod on top of the sample and data are gained using the thermo-dilatometric analysis (TDA), see ref. 39–42.

Elastic property measurements

Resonant ultrasound spectroscopy (RUS) outlined by Migliori *et al.*[43] was used to determine the elastic properties. For this

measurement, the cylindrically shaped samples of 10 mm diameter and masses between 2.5 g and 5 g were mounted "edge-to-edge" between two piezo-transducers and were excited *via* a network analyser in the 100 to 500 kHz frequency range at room temperature. Macroscopically, the polycrystalline samples are isotropic and the set of eigenfrequencies gained was then fitted providing the values for the Young's modulus E and Poisson's ratio ν.

Hardness measurements

The load-independent Vickers hardness HV was determined using an Anton Paar MHT 4 microhardness tester mounted on a Reichert POLYVAR microscope evaluating all the indentation data using eqn (2.2).

$$\mathrm{HV} = 2 \cdot F \frac{\sin\left(\frac{136°}{2}\right)}{d^2} \qquad (2.2)$$

F gives the indenter load and d is defined as

$$d = \frac{d_1 + d_2}{2} \qquad (2.3)$$

with d_1 and d_2 being the resulting diagonal lengths of the indenter, respectively.

Severe plastic deformation (SPD) *via* high-pressure torsion

The HPT technique is based on the use of a Bridgman anvil-type device. A thin disk-shaped sample was subjected to torsional strain in a cavity under high hydrostatic pressure between two anvils at room temperature or at elevated temperatures *via* induction heating. The shear strain γ is dependent on the number of revolutions n, the radius r, and the thickness t of the specimen in the following way:

$$\eta = \frac{2 \cdot \pi \cdot n \cdot r}{t} \qquad (2.4)$$

Therefore, the cylindrical single-phase samples were cut into slices with a thickness (t) of about ~1 mm and a diameter of 10 mm. The Sb-rich alloys were processed at 400 °C under a hydrostatic pressure of 4 GPa with 1 revolution, whereas the temperature for Sn-rich samples was only 300 °C.

DTA measurements

Melting points were determined from DTA measurements recorded on a NETZSCH STA 409 C/CD equipment. Pieces of single-phase samples weighing 500 mg to 600 mg were sealed in evacuated quartz glass crucibles. In general, three heating and three cooling curves were recorded for each sample using a scanning rate of 5 K min^{-1}.

Crystallite size evaluation

The crystallite size was evaluated from the X-ray diffraction patterns (spectra from Cu Kα_1 radiation) using the MDI JADE 6.0 software (Materials Data Inc., Liverpool, CA). This method yields the crystallite size from the full width at half maximum (FWHM) of a single diffraction peak using the Scherrer

formula.[44] Silicon was used as an internal standard for instrumental broadening. The calculations were performed for three well separated reflections, (240), (332) and (422), within a 2θ range from 51° to 58°. For details see ref. 45.

3. Filling levels, phase equilibria and homogeneity region

Phase equilibria in the ternary system Ni–Sn–Sb at 450 °C

For the binary boundary systems, we accepted the Ni–Sn phase diagram reported by Schmetterer *et al.*[46] and the Ni–Sb system reported by Cha *et al.*,[47] whereas the Sn–Sb phase diagram is consistent with a recent reinvestigation reported by Polt *et al.*[48]

Grytsiv *et al.* reported that the ternary skutterudite phase $Sn_yNi_4Sb_{12-x}Sn_x$ (τ) exhibits a wide range of homogeneity at 250 °C ($2.4 \leq x \leq 5.6$, $0 \leq y \leq 0.31$) and at 350 °C ($2.7 \leq x \leq 5.0$, $0 \leq y \leq 0.27$).[18] The phase equilibria change drastically by increasing the temperature from 250 to 350 °C and the authors[18] suggested that at least two invariant reactions exist in this temperature range. Mishra *et al.*[19] presented a detailed reaction scheme for the Sn-rich part of the system involving three invariant equilibria in the same temperature range. In order to derive the phase equilibria at 450 °C, we annealed several samples at this temperature for at least 30 days. Three-phase equilibria (Sb) + NiSb$_2$ + τ and NiSb$_2$ + α + τ at 450 °C (Fig. 1a and b) were found to be similar to those observed by Grytsiv *et al.* at 250 and 350 °C.[18] We also observed three-phase regions L + (Sb) + τ, L + α + τ, and L + Ni$_3$Sn$_2$ + α (Fig. 1c–e), which agree well with the Schultz-Scheil diagram derived by Mishra *et al.*[19]

The solid solution α (NiSb–Ni$_3$Sn$_2$) was observed in all the as-cast samples and has the widest liquidus field, likely being the most stable phase in the system. Thus, the as-cast alloy 2.7Ni–24.7Sn–72.6Sb shows primary crystallisation of the alpha-phase, which is surrounded by NiSb$_2$ and the last portion of liquid crystallizes with the composition 40Sn–60Sb. At 450 °C, the sample is in solid–liquid state (Fig. 1c): huge grains of the skutterudite (Ni$_4$Sb$_{9.1}$Sn$_{2.9}$) and antimony (Sb) were grown in equilibrium with the liquid with the composition 0.3Ni–47.75Sn–51.95Sb. Three-phase equilibria with the liquid phase L + Ni$_3$Sn$_4$ + α and L + α + τ are also well confirmed *via* investigation of the samples 21.5Ni–25.5Sn–53Sb and 35Ni–52Sn–13Sb (Fig. 1d and e). Between these two phase triangles, a huge two-phase field arises containing an Sn-rich liquid and the α-phase (Fig. 1f). The latter solid solution, formed by congruent melting compounds, separates the phase diagram into two subsystems for which the phase equilibria may be investigated independently. The equilibria in the Ni–NiSb–Ni$_3$Sn$_2$ subsystem have not been reinvestigated but were introduced after Burkhardt and Schubert (Fig. 2).[49]

The composition and lattice parameters of the skutterudite phase τ coexisting in the various three-phase equilibria at 450 °C are listed in Table 1. The isothermal section at 450 °C is shown in Fig. 2. At 450 °C, the homogeneity region of the ternary skutterudite phase τ-Sn$_y$Ni$_4$Sb$_{12-x}$Sn$_x$ extends for $2.4 \leq$
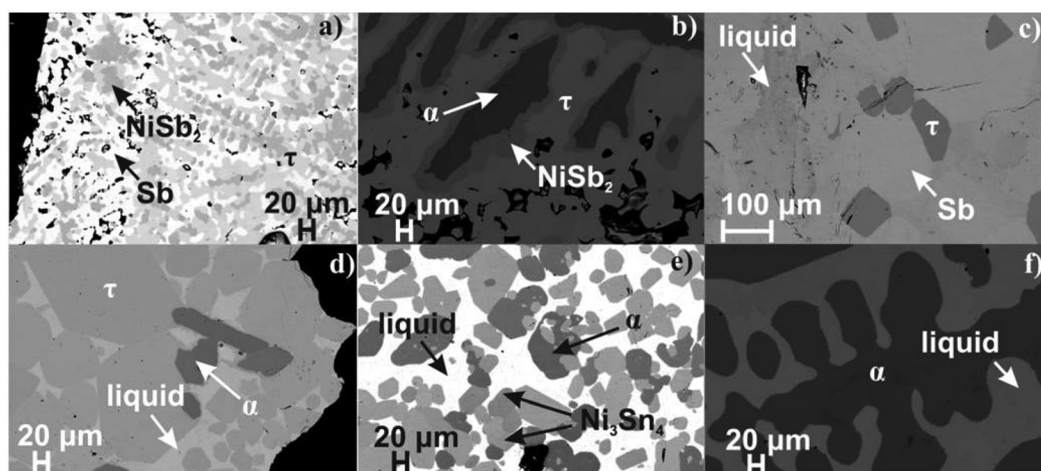
Fig. 1 Microstructure of Ni−Sn−Sb alloys annealed at 450 °C. The nominal composition (at% from EPMA) and X-ray phase analyses are given in Table 1.
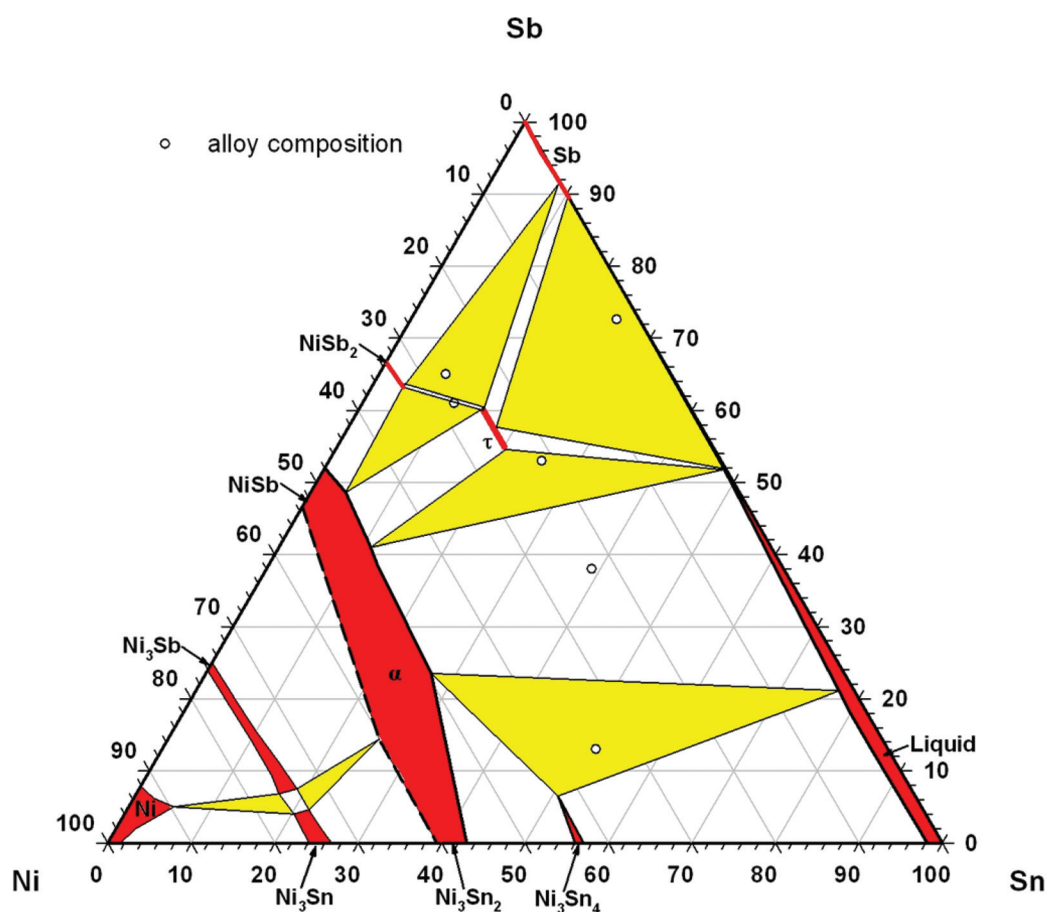

Fig. 2 Isothermal section of the Ni−Sn−Sb system at 450 °C. The microstructure of the investigated alloys is given in Fig. 1. The phase equilibria in the (Ni)−NiSb−Ni$_3$Sn$_2$ subsystem are shown by Burkhardt and Schubert.[49]
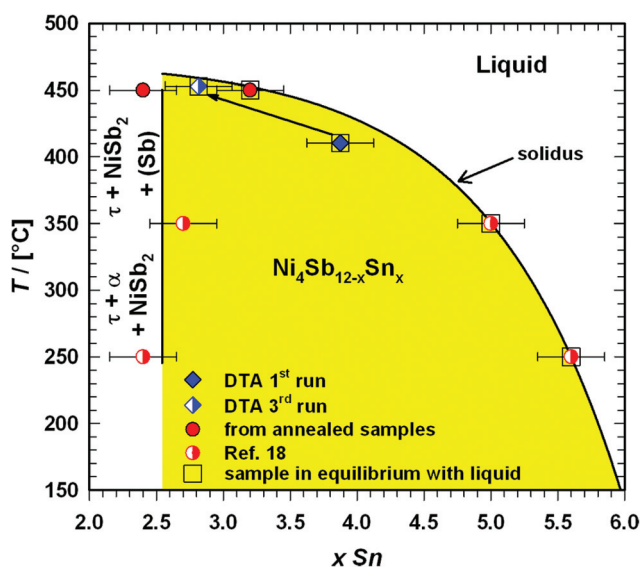
$x \leq 3.2$. By comparing the compositions of the ternary skutterudites Ni$_4$Sb$_{12-x}$Sn$_x$ as a function of the Sn-content from the homogeneity regions at 250 °C and 350 °C[18] as well as at 450 °C with those after DTA, a good agreement was found (see Fig. 3).

One may see a weak temperature dependence for the Sb-rich end of the skutterudite solid solution that coexists in three-phase solid-state equilibria: (Sb) + NiSb$_2$ + τ and NiSb$_2$ + α + τ. However, the Sn-rich side of the homogeneity region in

Table 1 Three-phase equilibria, lattice parameter and phase composition of the alloys in the Ni−Sn−Sb system

Phase region	Phase	Composition (EPMA; at%)			Formula (normalized to Ni = 4 and (Sb + Sn) = 12) $Ni_4Sb_{12-x}Sn_x$	a [nm]	ρ_X [g cm^{-3}]
		Ni	Sb	Sn			
(Sb) + NiSb$_2$ + τ	(Sb)	—	95.4	4.6	—	—	—
	NiSb$_2$	33.8	64.8	1.4	—	—	—
	τ	24.6	60.5	15.0	$Ni_4Sb_{9.6}Sn_{2.4}$	0.91360(11)	7.492
NiSb$_2$ + α + τ	NiSb$_2$	32.7	63.4	3.9	—	—	—
	α	47.2	48.6	4.2	—	—	—
	τ	24.7	60.4	15.0	$Ni_4Sb_{9.6}Sn_{2.4}$	0.91309(4)	7.488
L + (Sb) + τ	L	0.3	52.0	47.8	—	—	—
	(Sb)	—	89.7	10.3	—	—	—
	τ	24.3	57.5	18.2	$Ni_4Sb_{9.1}Sn_{2.9}$	0.90608(10)	7.421
L + α + τ	L	0.4	51.8	47.8	—	—	—
	α	48.0	41.0	11.0	—	—	—
	τ	24.5	55.2	20.4	$Ni_4Sb_{8.8}Sn_{3.2}$	0.91128(3)	7.538
L + α + Ni$_3$Sn$_4$	L	1.8	21.1	77.1	—	—	—
	α	49.5	23.5	27.0	—	—	—
	Ni$_3$Sn$_4$	42.8	6.5	50.7	—	—	—

Fig. 3 Temperature dependent extent and solidus curve of the ternary skutterudite phase τ-$Ni_4Sb_{12-x}Sn_x$.

equilibrium with the liquid phase shows a significant temperature dependence. With increasing temperature, the composition of the liquid gets strongly depleted on Sn, resulting in a pronounced phase segregation during the crystallization of the samples. DTA of the single-phase sample $Ni_4Sb_{8.2}Sn_{3.8}$ (Fig. 4a) reveals a solidus temperature of 410 °C during the first heating (Fig. I of the ESI‡ and Table 2); however, the temperature was increased to 453 °C after the second and third heating cycles (see Fig. I of the ESI‡). Further additional thermal effects appear in the temperature range from 415 to 423 °C. EPMA of the sample after DTA (Fig. 5a) shows three phases α, β (SnSb) and skutterudite τ with an Sb-enriched composition ($Ni_4Sb_{8.9}Sn_{3.1}$).

Homogeneity region for the filled skutterudite $Ba_yNi_4Sb_{12-x}Sn_x$

In general, the filling of the 2a site in the skutterudite structure has a maximal effect on the reduction of the lattice thermal conductivity.[6,28] In order to define the solubility of the electropositive filler (Ba) in $Ni_4Sb_{12-x}Sn_x$, two samples with nominal compositions of 1Ba–4Ni–5Sb–7Sn and 1Ba–4Ni–8Sb–4Sn were investigated in the as-cast state and after annealing at 250, 350 and 450 °C.

Rietveld refinements for the occupancy in the 2a site in combination with EPMA measurements are shown in Fig. 6. No skutterudites were observed in the as-cast alloys. The skutterudite phase is formed after annealing and appears in the microstructure as the main phase for one of the three temperatures 250, 350 or 450 °C (Fig. 7). In all cases, we observed an increase in the filling level with increasing Sn-content reaching $y = 0.93$ for the Ba filled skutterudite, while Fig. 7 additionally shows a clear dependence of the filling level on the temperature. Furthermore, for the Sn-rich compositions, EPMA reveals two sets of skutterudite compositions in the samples annealed at 350 °C and 450 °C. Such phase segregation is not likely connected with diffusion, suppressed at these temperatures, because the heat treatment at 250 °C yields the formation of a skutterudite with a uniform composition. Considering the interesting behaviour of the Ba filled skutterudite, this compound was selected for detailed investigations at 450 °C.

For several quaternary samples, annealed at 450 °C, the Ba filling level in dependence of the Sn content was determined by Rietveld refinements combined with microprobe measurements and yielded a large homogeneity region of $Ba_yNi_4Sb_{12-x}Sn_x$, as shown in a two-dimensional (2D) projection in Fig. 8. Obviously, the maximal solubility of Ba in the skutterudite ($y > 0.93$) responds to two cases: (i) an equilibrium with the Sn-rich liquid and (ii) the crystallization of skutterudites with two compositions ($Ba_{0.94}Ni_4Sb_{6.1}Sn_{5.9}$ and

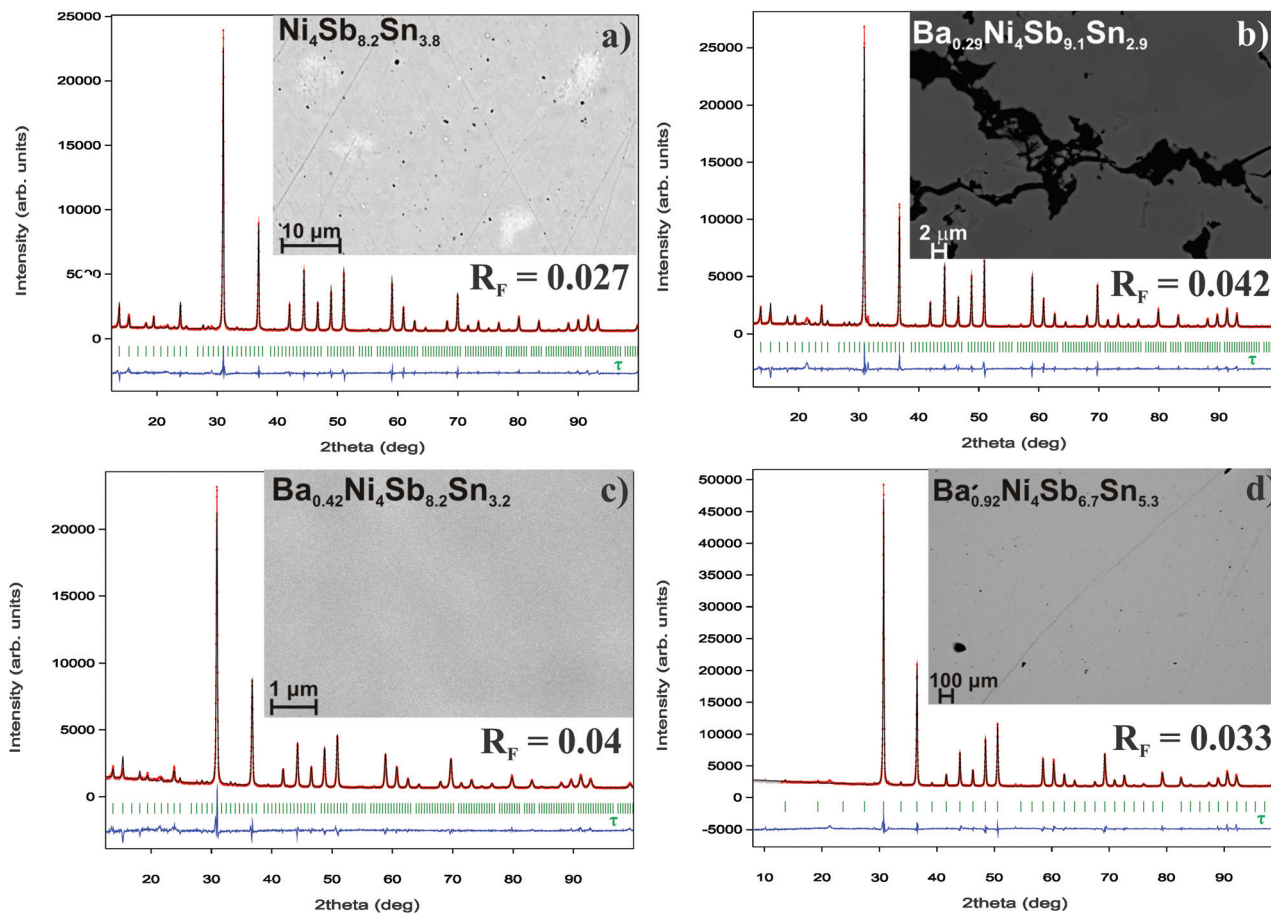**Fig. 4** Microstructure and Rietveld refinements for the single-phase samples of (a) $Ni_4Sb_{8.2}Sn_{3.8}$, (b) $Ba_{0.29}Ni_4Sb_{9.1}Sn_{2.9}$, (c) $Ba_{0.42}Ni_4Sb_{8.2}Sn_{3.8}$ and (d) $Ba_{0.92}Ni_4Sb_{6.7}Sn_{5.3}$.
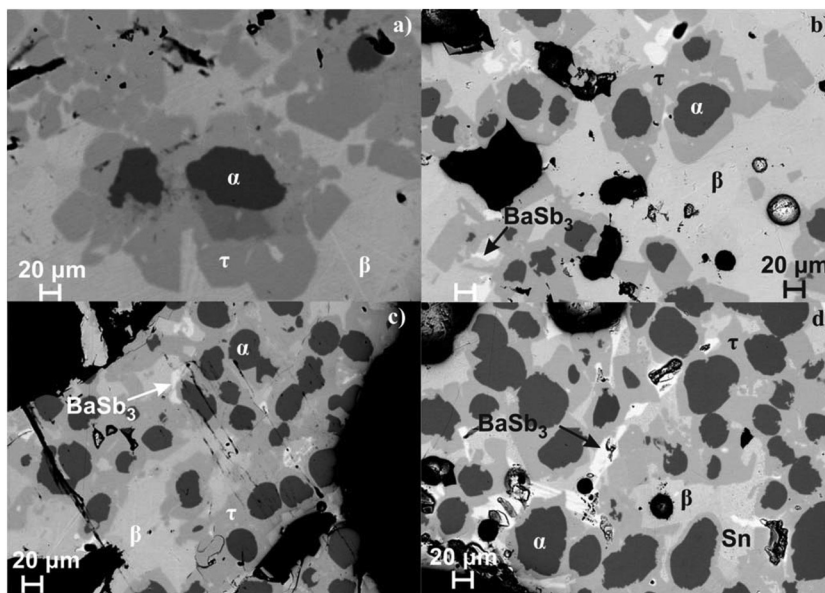
Fig. 5 Microstructure of the single-phase samples of (a) $Ni_4Sb_{8.2}Sn_{3.8}$, (b) $Ba_{0.29}Ni_4Sb_{9.1}Sn_{2.9}$, (c) $Ba_{0.42}Ni_4Sb_{8.2}Sn_{3.8}$ and (d) $Ba_{0.92}Ni_4Sb_{6.7}Sn_{5.3}$ after DTA (τ denotes the skutterudite phase $Ba_yNi_4Sb_{12-x}Sn_x$, α the continuous solid solution $NiSb-Ni_3Sn_2$ and β the binary compound SnSb).

Table 2 Composition-dependent melting points T_m of the filled and unfilled Ni–Sn–Sb based skutterudites

Composition				Formula	T_m [°C]
(EPMA; at%)				(Normalized to Ni = 4 and (Sb + Sn) = 12)	
Ba	Ni	Sb	Sn	$Ni_4Sb_{12-x}Sn_x$	From DTA
—	24.6	55.8	19.6	$Ni_4Sb_{8.9}Sn_{3.1}$	453
—	24.5	51.9	23.6	$Ni_4Sb_{8.2}Sn_{3.8}$	410
1.8	24.2	56.1	17.9	$Ba_{0.29}Ni_4Sb_{9.2}Sn_{2.9}$	534
3.2	23.8	57.1	15.9	$Ba_{0.55}Ni_4Sb_{9.4}Sn_{2.6}$	521
2.5	23.9	50.4	23.2	$Ba_{0.42}Ni_4Sb_{8.2}Sn_{3.8}$	533
3.6	23.8	52.5	20.1	$Ba_{0.61}Ni_4Sb_{8.7}Sn_{3.3}$	540
5.1	23.6	42.1	29.1	$Ba_{0.87}Ni_4Sb_{7.1}Sn_{4.9}$	557
5.4	23.4	39.6	31.6	$Ba_{0.92}Ni_4Sb_{6.7}Sn_{5.3}$	554
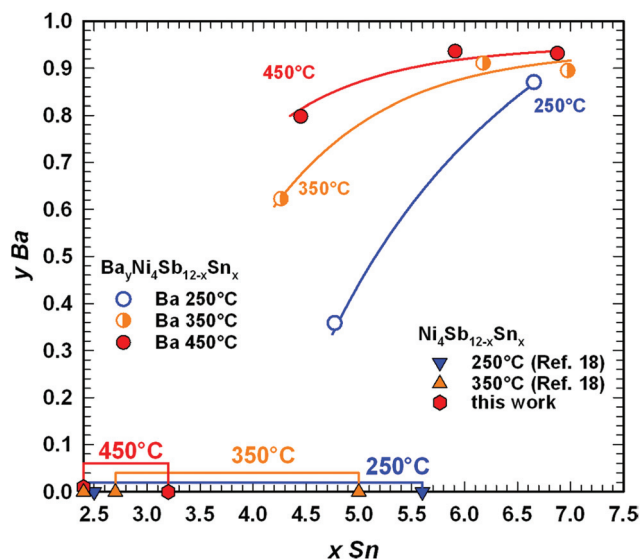
Fig. 6 Compositional dependence of the Ba filling level in $Ba_yNi_4Sb_{12-x}Sn_x$ at 250, 350 and 450 °C on the Sn-rich boundary of the skutterudite solid solution, as determined in the samples of 1Ba–4Ni–5Sb–7Sn and 1Ba–4Ni–8Sb (for their microstructures see Fig. 7).

$Ba_{0.93}Ni_4Sb_{5.1}Sn_{6.9}$) that coexist with Ni_3Sn_4. Upon increasing the Sb-content, the solubility decreases to $y = 0$ in the three-phase equilibria with (Sb) and $NiSb_2$ as well as with α and $NiSb_2$.

DTA provided further information on the stability of $Ba_yNi_4Sb_{12-x}Sn_x$. Three single-phase samples were used: $Ba_{0.42}Ni_4Sb_{8.2}Sn_{3.8}$ and $Ba_{0.92}Ni_4Sb_{6.7}Sn_{5.3}$ (Fig. 4c and d) after ball milling and hot pressing, and the compound $Ba_{0.29}Ni_4Sb_{9.1}Sn_{2.9}$, which appeared to be a single-phase after annealing at 450 °C (Fig. 4b). For these alloys, three heating and three cooling curves were recorded using a scanning rate of 5 K min^{-1} (see Fig. II to IV of the ESI‡). In all the first heating curves, only one signal could be detected; however, at lower temperatures, the subsequent heating and cooling curves revealed additional thermal effects associated with the incongruent melting of the alloys (also see Table 2). This was confirmed by the microstructure of the samples after DTA

(Fig. 5b–d). In all cases, we observe the formation of a high melting α-phase with subsequent crystallization of the β-phase and $BaSb_3$. A tin-rich liquid was found to form during crystallisation of $Ba_{0.92}Ni_4Sb_{6.7}Sn_{5.3}$. Due to incongruent crystallization of $Ba_yNi_4Sb_{12-x}Sn_x$, the composition of the skutterudite phase changes similarly to the ternary Ni–Sn–Sb skutterudite (see chapter above). The melting points, T_m, for the samples before and after DTA are listed in Table 2 and the compositional dependences of the solidus temperature were compared with data for the Ni–Sb–Sn skutterudite in Fig. 9. The filling of the skutterudite lattice with Ba-atoms clearly results in a significant increase in the melting temperature and this influence is particularly visible for the Sn-rich samples.

Knowledge of the extension of the homogeneity region for $Ba_yNi_4Sb_{12-x}Sn_x$ as a function of temperature was used to prepare single-phase samples for measurements of their physical properties (Fig. 4a, c, d and Table 3) and to grow single crystals for structural investigations.

4. Crystal structure and vibration modes of $Ba_yNi_4Sb_{12-x}Sn_x$

Rietveld refinements of the X-ray powder data for $Ba_yNi_4Sb_{12-x}Sn_x$ were fully consistent with the skutterudite structure $CoAs_3$ in the unfilled case and $LaFe_4Sb_{12}$ in the filled case. The refinements combined with EPMA defined the degree of filling in the 2a site and the Sb/Sn ratio in the 24g site. The compositional data and corresponding lattice parameters for all new phases of $Ba_yNi_4Sb_{12-x}Sn_x$ are summarized in Table 4. The lattice parameters revealed neither a dependence on the filling level of Ba nor on the Sb/Sn ratio.

For two flux-grown single crystals, $Ba_yNi_4Sb_{12-x}Sn_x$ (for details see micrographs in Fig. 10), the X-ray diffraction intensities were recorded at three different temperatures (100, 200 and 300 K). The refinement in all cases proved isotypism with the $LaFe_4Sb_{12}$ type (filled skutterudite; space group $Im\bar{3}$) with Ni atoms occupying the 8c site, whereas Sb and Sn atoms randomly share the 24g site. The residual density at the 2a site was assigned to Ba atoms. The compositions derived from the structural refinement, namely, $Ba_{0.73}Ni_4Sb_{8.1}Sn_{3.9}$ and $Ba_{0.95}Ni_4Sb_{6.1}Sn_{5.9}$, are in accordance with the microprobe measurements. Final refinements with fixed occupancies (Tables 5 and 6) and anisotropic atom displacement parameters (ADPs) led to a reliability factor R_F below 2%. The maximum residual electron density of ~3 e$^-$ Å^{-3} appears at a distance of 1.5 Å from the centre of the 24g site. This density can be interpreted as a "diffraction ripple" of the Fourier series around the heavy Sb and Sn atoms located at this site. The interatomic distances for Ni and (Sn/Sb) lie within range of values known for $CoSb_3$[15] and $LaFe_4Sb_{12}$.[52]

Fig. 11 shows the temperature dependence of the ADP for $Ba_{0.73}Ni_4Sb_{8.1}Sn_{3.9}$ and $Ba_{0.95}Ni_4Sb_{6.1}Sn_{5.9}$. Filler atoms in cage compounds such as skutterudites generally exhibit ADPs at RT, which are about three to four times higher than those of the framework atoms.[6] In the case of $Ba_yNi_4Sb_{12-x}Sn_x$, this
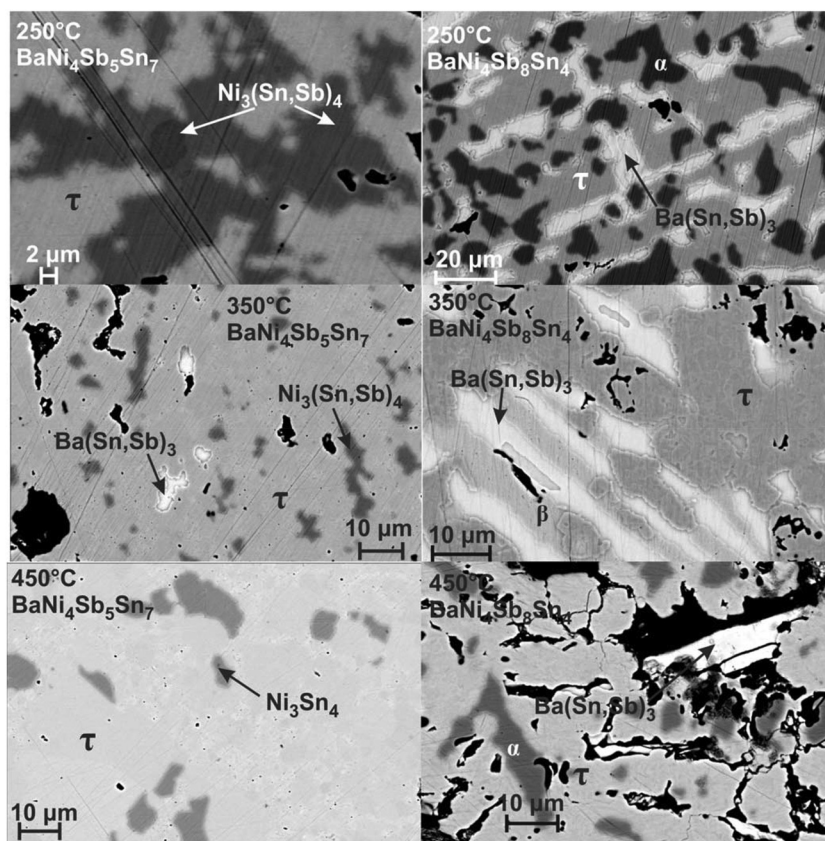
Fig. 7 Microstructure of the alloys $BaNi_4Sb_5Sn_7$ and $BaNi_4Sb_8Sn_4$, annealed at 250, 350 and 450 °C (τ denotes the skutterudite phase $Ba_yNi_4Sb_{12-x}Sn_x$, α the continuous solid solution $NiSb-Ni_3Sn_2$ and β the binary compound SnSb).

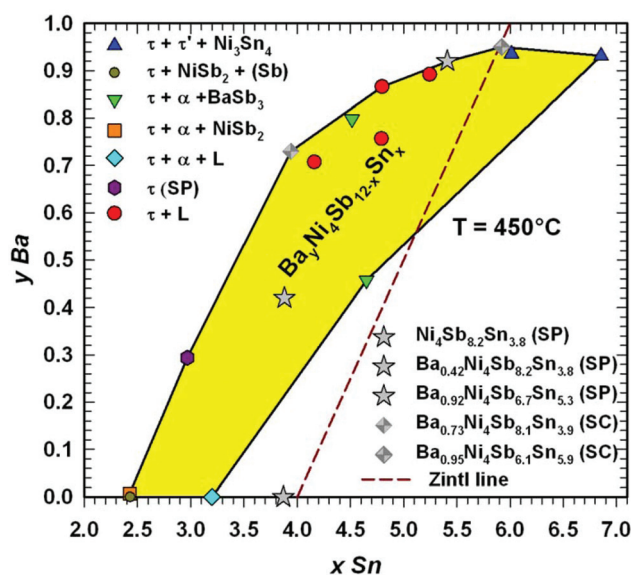**Fig. 8** Homogeneity region for $Ba_yNi_4Sb_{12-x}Sn_x$ at 450 °C as a function of Sn-content and Ba filling level. The composition of the single crystals (SC) and samples prepared for investigation of their physical properties (SP) are added. The ternary single-phase sample $Ni_4Sb_{8.2}Sn_{3.8}$ was found to be outside the estimated homogeneity region because the temperature during its preparation was about 10 °C below 450 °C.
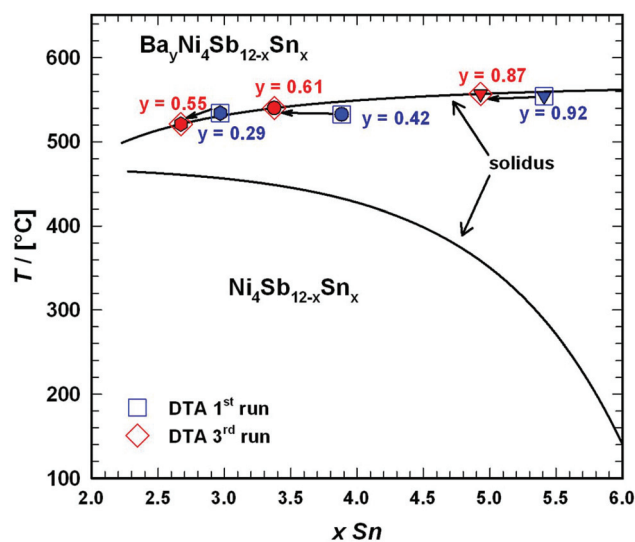

Fig. 9 Compositional dependence of the solidus curve for $Ba_yNi_4Sb_{12-x}Sn_x$ in comparison to that of $Ni_4Sb_{12-x}Sn_x$ (for details see Fig. 3). For the melting temperatures, see Table 2.

factor is only slightly above 1.2. Despite their low ADPs, the Ba atoms may be tentatively described as harmonic Einstein oscillators uncoupled from a framework that behaves as a Debye

Table 3 Composition, densities and lattice parameters of the samples used for the investigation of the physical and mechanical properties

Composition				Formula (Normalized to Ni = 4 and (Sb + Sn) = 12) $Ni_4Sb_{12-x}Sn_x$	a [nm]	ρ_X [g cm^{-3}]	ρ_s [g cm^{-3}]	ρ_s/ρ_X
(EPMA; at%)								
Ba	Ni	Sb	Sn					
—	24.45	51.87	23.60	$Ni_4Sb_{8.2}Sn_{3.8}$	0.91071(2)	7.598	7.490	0.99
2.52	23.89	50.4	23.19	$Ba_{0.42}Ni_4Sb_{8.2}Sn_{3.8}$	0.91418(4)	7.742	7.562	0.98
5.37	23.38	39.62	31.63	$Ba_{0.92}Ni_4Sb_{6.7}Sn_{5.3}$	0.91999(5)	7.800	7.686	0.99

Table 4 Composition and lattice parameters of the skutterudites $Ba_yNi_4Sb_{12-x}Sn_x$ for the single crystals,[a] single phase[b] and multiphase[c] alloys

Composition				Formula (Normalized to Ni = 4 and (Sb + Sn) = 12) $Ni_4Sb_{12-x}Sn_x$	a [nm]	ρ_X [g cm^{-3}]
(EPMA; at%)						
Ba	Ni	Sb	Sn			
—	24.6	60.5	15.0	$N_4Sb_{9.6}Sn_{2.4}$ [c]	0.91360(11)	7.492
—	24.7	60.4	15.0	$Ni_4Sb_{9.6}Sn_{2.4}$ [c]	0.91309(4)	7.488
—	24.3	57.5	18.2	$Ni_4Sb_{9.1}Sn_{2.9}$ [c]	0.90608(10)	7.421
—	24.5	55.2	20.4	$Ni_4Sb_{8.8}Sn_{3.2}$ [c]	0.91128(3)	7.538
1.8	24.2	56.1	17.9	$Ba_{0.29}Ni_4Sb_{9.2}Sn_{2.9}$ [b]	0.91343(5)	7.657
2.7	23.7	46.2	27.5	$Ba_{0.46}Ni_4Sb_{7.5}Sn_{4.5}$ [c]	0.91503(20)	7.807
4.1	23.4	48.2	24.3	$Ba_{0.7}1Ni_4Sb_8Sn_4$ [c]	0.91813(3)	7.855
4.3	23.6	48.8	23.3	$Ba_{0.73}Ni_4Sb_{8.1}Sn_{3.9}$ [a]	0.91995(2)	7.612
4.4	23.3	44.5	27.9	$Ba_{0.76}Ni_4Sb_{7.4}Sn_{4.6}$ [c]	0.91854(9)	7.882
4.7	23.6	45.1	26.6	$Ba_{0.80}Ni_4Sb_{7.6}Sn_{4.4}$ [c]	0.92183(74)	7.690
5.0	23.3	43.7	28.0	$Ba_{0.87}Ni_4Sb_{7.3}Sn_{4.7}$ [c]	0.92029(3)	7.834
5.2	23.3	41.0	30.5	$Ba_{0.89}Ni_4Sb_{6.9}Sn_{5.1}$ [c]	0.92024(38)	7.830
5.5	23.3	36.1	35.1	$Ba_{0.94}Ni_4Sb_{6.1}Sn_{5.9}$ [c]	0.92016(4)	7.805
5.5	23.7	30.2	40.6	$Ba_{0.93}Ni_4Sb_{5.1}Sn_{6.9}$ [c]	0.92016(4)	7.664
5.6	23.5	36.1	34.8	$Ba_{0.95}Ni_4Sb_{6.1}Sn_{5.9}$ [a]	0.92083(2)	7.692
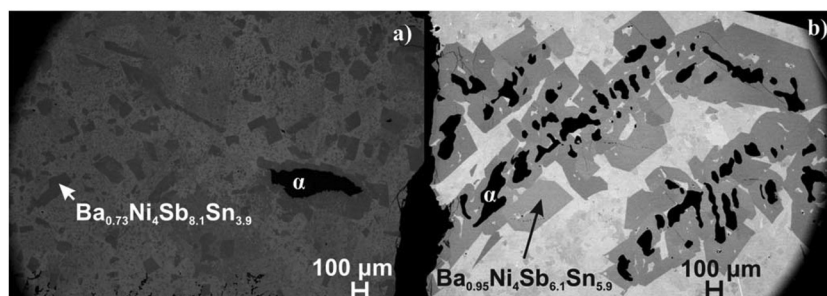
Fig. 10 Microstructure of the slowly cooled reguli used to grow the single crystals from the (a) (SnSb)-flux and (b) (Sn)-flux (α denotes the continuous solid solution of NiSb–Ni$_3$Sn$_2$).

solid. Least squares fitting of the temperature dependent ADPs of the Ba-atom, U_{eq} (isotropic by symmetry) with the Einstein model (eqn (4.1)) yields an Einstein temperature of 104 K for $Ba_{0.73}Ni_4Sb_{8.1}Sn_{3.9}$ and 111 K for $Ba_{0.95}Ni_4Sb_{6.1}Sn_{5.9}$. Similarly, the Debye model (eqn (4.2)) applied to the framework atoms (Ni, Sb and Sn) revealed only slight differences between θ_D for Ni and the random Sn/Sn mixture.

$$U_{eq} = \frac{\hbar}{2 \cdot m \cdot k_B \cdot \theta_{E,eq}} \cdot \coth\left(\frac{\theta_{E,eq}}{2 \cdot T}\right) \quad (4.1)$$

$$U_{eq} = \frac{3 \cdot \hbar^2 \cdot T}{m \cdot k_B \cdot \theta_D^2} \cdot \left[\frac{T}{\theta_D} \cdot \int_0^{\theta_D/T} \frac{x}{e^x - 1}\,dx + \frac{\theta_D}{4 \cdot T}\right] \quad (4.2)$$

θ_E and θ_D are listed in Table 7. As the skutterudite framework is built by the Sn and Sb atoms forming octahedra with the Ni atoms in the octahedral centres, one may explain these results as follows: because of its position in an octahedral cage formed by Sb and Sn, the vibration of the strongly bonded Ni atom is not independent from that of the framework and therefore leads to values close to those obtained for Sb/Sn.

Table 5 The X-ray single crystal data for skutterudite $Ba_{0.73}Ni_4Sb_{8.26}Sn_{3.94}$ (MoK_α radiation; standardized with program *Structure Tidy*;[50] temperature data for 100 K, 200 K and 300 K; redundancy >8); space group $Im\bar{3}$; no. 204. ADP (U_{ij}) are given in [10^{-2} nm^2]

Parameter	100 K	200 K	300 K
Space group	$Im\bar{3}$	$Im\bar{3}$	$Im\bar{3}$
Composition from EPMA[a]	$Ba_{0.73}Ni_4Sb_{8.1}Sn_{3.9}$	$Ba_{0.73}Ni_4Sb_{8.1}Sn_{3.9}$	$Ba_{0.73}Ni_4Sb_{8.1}Sn_{3.9}$
Composition from refinement	$Ba_{0.79}Ni_4Sb_{8.1}Sn_{3.9}$	$Ba_{0.78}Ni_4Sb_{8.1}Sn_{3.9}$	$Ba_{0.78}Ni_4Sb_{8.1}Sn_{3.9}$
Crystal size	$50 \times 20 \times 20$ μm^3	$50 \times 20 \times 20$ μm^3	$50 \times 20 \times 20$ μm^3
a [nm]	0.91791(2)	0.91887(2)	0.91995(2)
μ_{abs} [mm^{-1}]	27.24	24.80	27.06
ρ_x (g cm^{-3})	7.819	7.292	7.768
Data collection, 2θ range (°)	$2 \leq 2\theta \leq 72.6$; 100 s per frame	$2 \leq 2\theta \leq 72.6$; 100 s per frame	$2 \leq 2\theta \leq 72.6$; 100 s per frame
Total number of frames	240 for 6 sets; scan width = 2°	240 for 6 sets; scan width = 2°	240 for 6 sets; scan width = 2°
Reflections in refinement [total # of reflections]	$338 \geq 4\sigma(F_o)$ of 354 [609]	$339 \geq 4\sigma(F_o)$ of 354 [609]	$329 \geq 4\sigma(F_o)$ of 354 [610]
Mosaicity	<0.45	<0.45	<0.45
Number of variables	12	12	12
$R1_F = \sum|F_o - F_c|/\sum F_o$	0.0193	0.0203	0.0221
R_{Int}	0.0079	0.0078	0.0089
w$R2$	0.0328	0.0375	0.0485
GOF	1.181	1.178	1.133
Extinction (Zachariasen)	0.00117(5)	0.00117(6)	0.00118(10)
Ba in 2a (0,0,0); occ. = 0.79			
U_{11}; U_{22}; U_{33}	0.0043(3); 0.0043(3); 0.0043(3)	0.0071(3); 0.0071(3); 0.0071(3)	0.0105(3); 0.0105(3); 0.0105(3)
Ni in 8c ($\frac{1}{4}$, $\frac{1}{4}$, $\frac{1}{4}$); occ. = 1			
U_{11}; U_{22}; U_{33}; U_{23}; U_{13}; U_{12}	0.0058(1); 0.0040(1); 0.0040(1); 0.0002(1); 0.0002(1); 0.0002(1)	0.0058(2); 0.0058(2); 0.0058(2); 0.0004(1); 0.0004(1); 0.0004(1)	0.0078(2); 0.0078(2); 0.0078(2); 0.0005(1); 0.0005(1); 0.0005(1);
Sb in 24g (0, y, z); occ. = 0.68	0.16094(2); 0.34111(2)	0.16101(3); 34 114(3)	0.16110(3); 0.34119(3)
U_{11}; U_{22}; U_{33}; U_{23}	0.0029(1); 0.0036(1); 0.0073(1); 0.0006(1)	0.0048(1); 0.0065(1); 0.0098(1); 0.0007(1)	0.0068(1); 0.0093(1); 0.0127(1); 0.0008(1)
Sn in 24g (0, y, z); occ. = 0.32	0.16094(2); 0.34111(2)	0.16101(3); 0.34144(3)	0.16110(3); 0.34119(3)
U_{11}; U_{22}; U_{33}; U_{23}	0.0030(2); 0.0040(1); 0.0073(1); 0.0006(1)	0.0048(1); 0.0065(1); 0.0098(1); 0.0007(1)	0.0068(1); 0.0093(1); 0.0127(1); 0.0008(1)
Residual density; max; min [e$^-$ nm^{-3}]	2.03×10^3 (0.149 nm from Sb1/Sn1); -1.23×10^3 (0.160 nm from Sb1/Sn1)	2.10×10^3 (0.149 nm from Sb1/Sn1); -1.24×10^3 (0.161 nm from Sb1/Sn1)	2.66×10^3 (0.150 nm from Sb1/Sn1); -1.55×10^3 (0.051 nm from Sb1/Sn1)
Principal mean square atomic displacements U; U_{eq}	Ba: 0.0043 0.0043 0.0043; 0.0043(3) Ni: 0.0044 0.0037 0.0037; 0.0040(1) Sb: 0.0074 0.0038 0.0029; 0.0047(1) Sn: 0.0074 0.0038 0.0029; 0.0047(1)	Ba: 0.0071 0.0071 0.0071; 0.0071(3) Ni: 0.0065 0.0055 0.0055; 0.0058(2) Sb: 0.0100 0.0063 0.0048; 0.0070(1) Sn: 0.0100 0.0063 0.0048; 0.0070(1)	Ba: 0.0043 0.0043 0.0043; 0.0105(3) Ni: 0.0044 0.0037 0.0037; 0.0078(2) Sb: 0.0074 0.0038 0.0029; 0.0096(1) Sn: 0.0074 0.0038 0.0029; 0.0096(1)
Interatomic (standard deviations less than 0.0001 nm)[b]			
Ba 12 Sb/Sn	0.3462	0.3466	0.3471
20[c] 8 Ni	0.3975	0.3979	0.3984
Ni 6 Sb/Sn	0.2576	0.2578	0.2581
8 2 Ba	0.3975	0.3979	0.3984
Sb/Sn 2 Ni	0.2576	0.2578	0.2581
9 1 Sb/Sn	0.2917	0.2929	0.2922
1 Sb/Sn	0.2955	0.2959	0.2964
4 Sb/Sn	0.3437	0.3440	0.3443
1 Ba	0.3462	0.3466	0.3471

[a] Normalized to Ni = 4 and (Sn + Sb) = 12. [b] Gathered with the program DIDO_95.[51] [c] Coordination numbers.

While the Debye temperatures fit well (particularly for Sb/Sn), the Einstein temperatures are apparently lower than those of other filled skutterudites reported in the literature (see for example ref. 23) and hint towards a tightly bonded Ba-atom squeezed into a smaller $Ni_4(Sn,Sb)_{12}$ icosahedron in relation to those formed by the larger filled Co_4Sb_{12} cages. A calculation of the icosahedron volume (treated as a Voronoi polyhedron, calculated with the DIDO_95 program[51]) reveals 294.5 nm^3 for $Ba_{0.35}Co_4Sb_{12}$ with respect to only 289.7 nm^3 for $Ba_{0.73}Ni_4Sb_{8.1}Sn_{3.9}$.

By fitting the temperature dependent lattice parameters *via* a linear function of the form $a \cdot x + b$ (with $a = 1.02 \times 10^{-5}$ and $b = 0.92$ in the case of $Ba_{0.73}Ni_4Sb_{8.1}Sn_{3.9}$, but $a = 1.15 \times 10^{-5}$ and $b = 0.92$ for $Ba_{0.95}Ni_4Sb_{6.1}Sn_{5.9}$), the thermal expansion coefficients for the two compositions could also be determined (Table 7). All values for α lie within the range discovered for other skutterudites and increase with higher filling levels.[22,23]

5. Mössbauer spectroscopy

In order to access and quantify a potential occupation of the rattling 2a site by Sn, temperature dependent Mössbauer spectroscopy measurements were conducted for the ^{119}Sn resonance from 10 to 290 K. As potential Sn on the 2a site should be rather weakly bonded, a very low Lamb–Mössbauer factor

Table 6 The X-ray single crystal data for skutterudite $Ba_{0.73}Ni_4Sb_{8.26}Sn_{3.94}$ (MoK$_\alpha$ radiation; standardized with program *Structure Tidy*;[50] temperature data for 100 K, 200 K and 300 K; redundancy >8); space group $Im\bar{3}$ no. 204. ADP (U_{ij}) are given in [10^{-2} nm^2]

Parameter	100 K	200 K	300 K
Space group	$Im\bar{3}$	$Im\bar{3}$	$Im\bar{3}$
Composition from EPMA[a]	$Ba_{0.95}Ni_4Sb_{6.1}Sn_{5.9}$	$Ba_{0.95}Ni_4Sb_{6.1}Sn_{5.9}$	$Ba_{0.95}Ni_4Sb_{6.1}Sn_{5.9}$
Composition from refinement	$Ba_{0.99}Ni_4Sb_{6.1}Sn_{5.9}$	$Ba_{0.99}Ni_4Sb_{6.1}Sn_{5.9}$	$Ba_{0.99}Ni_4Sb_{6.1}Sn_{5.9}$
Crystal size	$80 \times 30 \times 30$ μm^3	$80 \times 30 \times 30$ μm^3	$80 \times 30 \times 30$ μm^3
a [nm]	0.91854(2)	0.91961(2)	0.92083(2)
μ_{abs} [mm^{-1}]	24.56	26.83	26.72
ρ_x (g cm^{-3})	7.275	7.750	7.719
Data collection, 2θ range (°)	$2 \leq 2\theta \leq 72.6$; 100 s per frame	$2 \leq 2\theta \leq 72.6$; 100 s per frame	$2 \leq 2\theta \leq 72.6$; 100 s per frame
Total number of frames	240 for 6 sets; scan width = 2°	240 for 6 sets; scan width = 2°	240 for 6 sets; scan width = 2°
Reflections in refinement [total # of reflections]	$354 \geq 4\sigma(F_o)$ of 359 [621]	$352 \geq 4\sigma(F_o)$ of 357 [618]	$343 \geq 4\sigma(F_o)$ of 354 [613]
Mosaicity	<0.45	<0.45	<0.45
Number of variables	12	12	12
$R1_F = \sum|F_o - F_c|/\sum F_o$	0.0171	0.0170	0.0197
R_{Int}	0.0112	0.0107	0.0122
w$R2$	0.0414	0.0416	0.0470
GOF	1.422	1.324	1.181
Extinction (Zachariasen)	0.00217(10)	0.00389(14)	0.01030(32)
Ba1 in 2a (0,0,0); occ. = 0.99			
U_{11}; U_{22}; U_{33}	0.0030(2); 0.0030(2); 0.0030(2)	0.0059(2); 0.0059(2); 0.0059(2)	0.0089(2); 0.0089(2); 0.0089(2)
Ni1 in 8c ($\frac{1}{4}$, $\frac{1}{4}$, $\frac{1}{4}$); occ. = 1			
U_{11}; U_{22}; U_{33}; U_{23}; U_{13}; U_{12}	0.0032(2); 0.0032(2); 0.0032(2); 0.0004(1); 0.0004(1); 0.0004(1)	0.0050(2); 0.0050(2); 0.0050(2); 0.0007(1); 0.0007(1); 0.0007(1)	0.0069(2); 0.0069(2); 0.0078(2); 0.0008(1); 0.0008(1); 0.0008(1);
Sb1 in 24g (0, y, z); occ. = 0.51	0.16241(2); 0.34238(2)	0.16252(2); 34 241(2)	0.16266(3); 0.34245(3)
U_{11}; U_{22}; U_{33}; U_{23}	0.0023(1); 0.0036(1); 0.0028(1); 0.00002(6)	0.0042(1); 0.0062(1); 0.0051(1); 0.0002(6)	0.0063(1); 0.0089(1); 0.0076(1); −0.0001(1)
Sn1 in 24g (0, y, z); occ. = 0.49	0.16241(2); 0.34238(2)	0.16252(2); 0.34241(2)	0.16266(3); 0.34245(3)
U_{11}; U_{22}; U_{33}; U_{23}	0.0023(1); 0.0036(1); 0.0028(1); 0.00002(6)	0.0042(1); 0.0062(1); 0.0051(1); 0.0002(6)	0.0063(1); 0.0089(1); 0.0076(1); −0.0001(1)
Residual density; max; min [e$^-$ nm^{-3}]	1.27×10^3 (0.077 nm from Sb1/Sn1); -1.12×10^3 (0.056 nm from Sb1/Sn1)	1.78×10^3 (0.151 nm from Sb1/Sn1); -1.63×10^3 (0.055 nm from Sb1/Sn1)	2.07×10^3 (0.152 nm from Sb1/Sn1); -1.78×10^3 (0.054 nm from Sb1/Sn1)
Principal mean square atomic displacements U; U_{eq}	Ba1: 0.0043 0.0043 0.0043; 0.0030(2); Ni1: 0.0044 0.0037 0.0037; 0.0032(2); Sb1: 0.0074 0.0038 0.0029; 0.0029(1); Sn1: 0.0074 0.0038 0.0029; 0.0029(1)	Ba1: 0.0059 0.0059 0.0059; 0.0059(2); Ni1: 0.0062 0.0043 0.0043; 0.0050(2); Sb1: 0.0062 0.0051 0.0042; 0.0052(1); Sn1: 0.0062 0.0051 0.0042; 0.0052(1)	Ba1: 0.0089 0.0089 0.0089; 0.0089(2); Ni1: 0.0086 0.0061 0.0061; 0.0069(2); Sb1: 0.0089 0.0076 0.0063; 0.0076(1); Sn1: 0.0089 0.0076 0.0063; 0.0076(1)
Interatomic (standard deviations less than 0.0001 nm)[b]			
Ba 12 Sb/Sn	0.3481	0.3486	0.3491
20[c] 8 Ni	0.3977	0.3982	0.3987
Ni 6 Sb/Sn	0.2577	0.2580	0.2583
8 2 Ba	0.3977	0.3982	0.3987
Sb/Sn 2 Ni	0.2577	0.2580	0.2583
9 1 Sb/Sn	0.2896	0.2898	0.2902
1 Sb/Sn	0.2984	0.2989	0.2996
4 Sb/Sn	0.3423	0.3426	0.3429
1 Ba	0.3481	0.3486	0.3491

[a] Normalized to Ni = 4 and (Sn + Sb) = 12. [b] Gathered with the program DIDO_95.[51] [c] Coordination numbers.

would be expected for the corresponding component, which necessitates the low temperature measurements. The ^{119}Sn Mössbauer spectra are shown in Fig. 12 and are basically characterized by a broad, slightly asymmetric doublet-like structure. The spectra were fitted with a model consisting of up to three doublets, which represent the different configurations of Sn on the 24g site with zero, one or two Sb next neighbors (NN). As for each Sn atom, the probability of two NN Sn atoms is above 0.1 only for sample $Ba_{0.92}Ni_4Sb_{6.7}Sn_{5.3}$, the Mössbauer spectra of the other samples were analyzed

using two doublets. Exemplarily, these different components are also shown in Fig. 12 for measurements at 290 K and the Mössbauer parameters of all components at all temperatures are summarized in Table I of the ESI.‡

With the exception of the $Ba_{0.92}Ni_4Sb_{6.7}Sn_{5.3}$ sample, which exhibits the highest filling fraction, component I (see Table I of the ESI‡) consistently shows the biggest quadrupole splitting, which can be related to the more covalent character of the bond[53] in the case of Sb NN. The average isomer shifts and quadrupole splittings are shown in Fig. 13 and reasonably
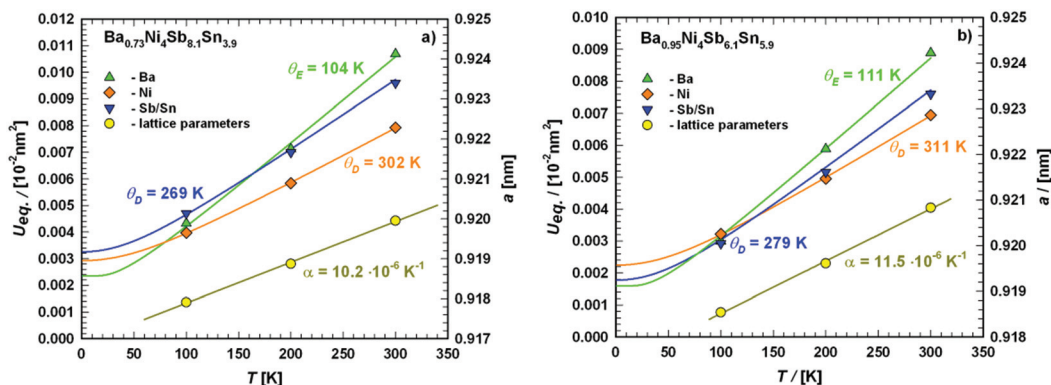
Fig. 11 Temperature dependence of the lattice parameter a (right axis) and the atomic displacement parameters (ADP) (left axis) of (a) $Ba_{0.73}Ni_4Sb_{8.1}Sn_{3.9}$ and (b) $Ba_{0.95}Ni_4Sb_{6.1}Sn_{5.9}$ obtained from the X-ray single-crystal measurements at 100, 200 and 300 K. The solid lines correspond to the least squares fitting according to eqn (4.1) and (4.2) for the ADPs and a simple linear fit for the thermal expansion coefficient.

Table 7 Comparison of Debye temperature θ_D, Einstein temperature θ_E and thermal expansion coefficients α gained using different experimental methods for various single crystalline (SC) and single phase (SP) $Ba_yNi_4Sb_{12-x}Sn_x$ skutterudites

Composition	Material	Method[b]	γ [mJ mol^{-1} K^{-1}]	θ_D [K]	θ_{E1}	θ_{E2}	θ_{E3}	Method[c]	$\alpha \times 10^{-6}$ [K^{-1}]
					θ_{Ei} [K]				
$Ba_{0.73}Ni_4Sb_{8.1}Sn_{3.9}$	SC	ADP		277[a]	104	—	—	LP	10.2
$Ba_{0.95}Ni_4Sb_{6.1}Sn_{5.9}$	SC	ADP		289[a]	111	—	—	LP	11.5
$Ni_4Sb_{8.2}Sn_{3.8}$	SP	MB		217	—	—	—	CD	11.8
		LTF	9	223	—	—	—	TDA	11.0
		DEM		264	71	—	534		
		JF		220	68	—	—		
		FER		220	—	—	—		
		FTC		224	—	—	—		
		FTE		223	—	—	—		
		RUS		252	—	—	—		
$Ba_{0.29}Ni_4Sb_{9.2}Sn_{2.9}$	SP	MB		229	—	—	—		
$Ba_{0.42}Ni_4Sb_{8.2}Sn_{3.8}$	SP	MB		244	—	—	—	CD	12
		LTF	15	265	—	—	—	TDA	11.8
		DEM		256	57	97	599		
		JF		256	54.1	81	—		
		FER		263	—	—	—		
		FTC		262	—	—	—		
		FTE		273	103	—	—		
		RUS		266	—	—	—		
$Ba_{0.92}Ni_4Sb_{6.7}Sn_{5.3}$	SP	MB		260	—	—	—	CD	13.2
		LTF	13.1	265	—	—	—	TDA	12.5
		DEM		255	60	102	599		
		JF		269	54.7	98.4	—		
		FER		261	—	—	—		
		FTC		264	—	—	—		
		FTE		278	100	—	—		
		RUS		270	—	—	—		

[a] The average Debye temperature calculated *via* $[\theta_D(Ni) + 3\cdot\theta_D(Sb/Sn)]/4$. [b] Method: ADP – fit of atomic displacement parameters; MB – fit of Lamb–Mössbauer factor; LTF – low temperature fit of C_p/T *vs.* T^2; DEM – combined Debye and Einstein model; JF – Junod fit; FER – fit of electrical resistivity; FTC – fit of thermal conductivity; FTE – fit of thermal expansion; RUS – resonant ultrasound spectroscopy. [c] Method: LP – fit of temperature dependent lattice parameters; CD – fit of capacitance dilatometer measurement data; TDA – fit of thermodilatometric analysis measurement data.

agree with the previously reported Mössbauer data on $Ni_4Sb_9Sn_3$.[18]

Notably, average isomer shifts and quadrupole splittings in the $Ba_{0.92}Ni_4Sb_{6.7}Sn_{5.3}$ sample significantly differ from the values obtained for the other compounds (see Fig. 13). Considering the available data, a correlation of Mössbauer parameters with the Ba- or Sn-content is, however, rather ambiguous. As there is no indication for a Mössbauer component with Einstein like behavior and/or significant contribution only at low temperature, which would be the case for Sn on the 2a site, the possibility of Sn on the rattling position is ruled out. The relative absorption area of a Mössbauer spectrum is pro-
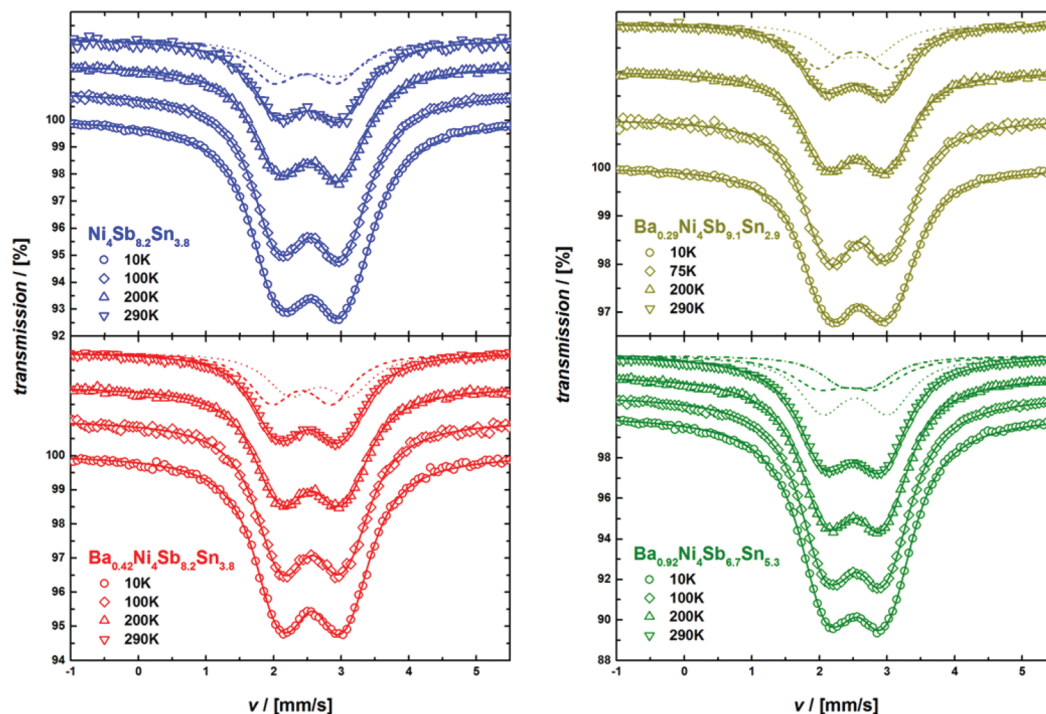
Fig. 12 ^{119}Sn-Mossbauer spectra obtained at different temperatures. The solid lines represent the corresponding fits. For the room temperature measurements, the different components I (dashed line), II (dotted line) and III (dot-and-dashed line) are also displayed (see text and Table I of the ESI‡ for further details).

portional to the Lamb–Mössbauer factor f_{LM} and thus, the temperature dependence of the former can be used to fit f_{LM} within a Debye model:[54]

$$f_{LM}(T) = \exp\left[-\frac{3E_\gamma{}^2}{k_B\theta_D Mc^2}\left(\frac{1}{4}+\frac{T^2}{\theta_D{}^2}\int_0^{\theta_D/T}\frac{x}{e^x-1}\mathrm{d}x\right)\right] \quad (5.1)$$

where E_γ is the Mössbauer resonance energy, M is the nuclear mass and θ_D is the Debye temperature (sometimes called

Mössbauer temperature in this context). For all four skutterudites, the results are displayed in Fig. 14 including the corresponding Debye temperatures. The latter values obtained from Mössbauer spectroscopy are in good agreement with the Debye temperatures based on the X-ray diffraction and heat capacity measurements (see Table 7). In particular, the hardening of the host lattice with increasing filling fraction is reflected in the fitted Debye temperatures and exhibits an almost linear dependency with a slope of about 55(11) K per Ba per f.u.
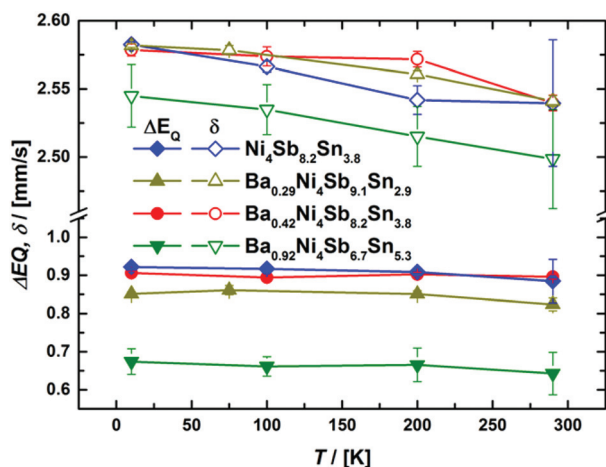
Fig. 13 Temperature dependent average isomer shift δ (top) and quadrupole splitting ΔE_Q (bottom) for the ^{119}Sn Mössbauer spectroscopy.

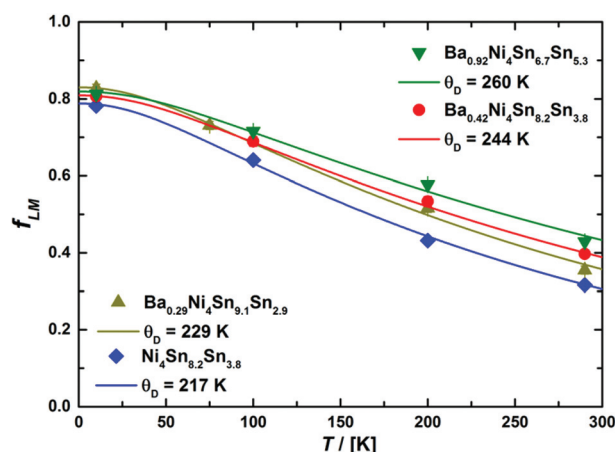**Fig. 14** Lamb–Mössbauer factors f_{LM} calculated from the relative absorption area within the Debye model (see text for further details).
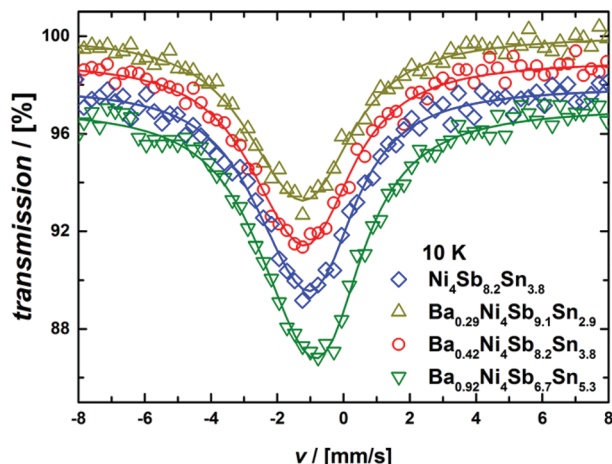
Fig. 15 ^{121}Sb Mössbauer spectra measured at 10 K. All fits (solid lines) were conducted with a fixed, vanishing asymmetry term.

Fig. 16 Temperature-dependent specific heat divided by temperature C_p/T for $Ni_4Sb_{8.2}Sn_{3.8}$, $Ba_{0.42}Ni_4Sb_{8.2}Sn_{3.8}$ and $Ba_{0.92}Ni_4Sb_{6.78}Sn_{5.41}$. The dashed lines correspond to the least squares fits according to eqn (6.5).

The ^{121}Sb-Mössbauer spectra obtained at 10 K are shown in Fig. 15. They are characterized by a single asymmetric peak, which in the case of ^{121}Sb indicates a quadrupole splitting. All the ^{121}Sb-spectra could be fitted with a single component. The corresponding Mössbauer parameters are summarized in Table II of the ESI.‡ Due to the rather large linewidth of the ^{121}Sb Mössbauer transition, linewidth, quadrupole splitting and the asymmetry term are highly correlated and particularly the asymmetry term cannot be reliably fitted. As fitting with a fixed, vanishing asymmetry term slightly improved the fitting quality when compared to fitting with a fixed, maximal asymmetry term, all the results presented herein were obtained with the vanishing asymmetry term. This aspect and the quadrupole splitting values are in contrast to the reports on $CoSb_3$ mentioned in ref. 55 and 56, which can, however, be attributed to the reduction of Sb content in the present samples. In any case, the present findings validate the sample quality from the Sb perspective.

6. Specific heat

To gather further information on the vibrational behavior of the filled and unfilled $Ba_yNi_4Sb_{12-x}Sn_x$ skutterudites, specific heat measurements in the temperature range from 3 to 140 K were applied to the single-phase specimens $Ni_4Sb_{8.2}Sn_{3.8}$, $Ba_{0.42}Ni_4Sb_{8.2}Sn_{3.8}$ and $Ba_{0.92}Ni_4Sb_{6.7}Sn_{5.3}$. The data are displayed in Fig. 16 in the form of a C_p/T versus T plot. The specific heat, C_p, of simple non-magnetic materials can be expressed as

$$C_p = C_{p,el} + C_{p,ph} = \gamma \cdot T + \beta \cdot T^3 \qquad (6.1)$$

with

$$\beta = \frac{12}{5} \cdot \frac{\pi^4 \cdot N_A \cdot k_B}{\theta_D^3} = \frac{1994 \cdot n}{\theta_D^3}. \qquad (6.2)$$
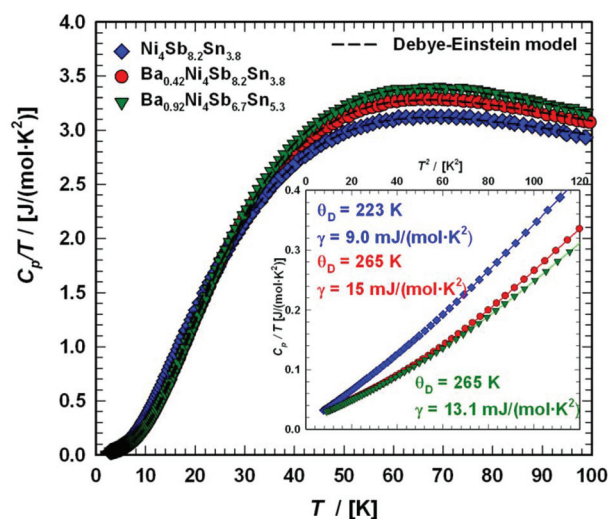
γ is the Sommerfeld coefficient and β is inversely proportional to θ_D. N_A is Avogadro's number, k_B is the Boltzmann factor and n stands for the number of atoms per formula unit. Table 7 summarizes the parameters obtained from the least square fitting below 5 K. Fig. 16 suggests a moderate overall lattice softening with increasing Ba and Sn content. To extract the corresponding Einstein temperatures and Einstein frequencies, the specific heat data were analysed by applying two different methods. The first approach was based on an additive combination of the Debye and Einstein models. It is assumed that the phonon spectrum of a polyatomic compound contains three acoustic branches and 3n-3 optical branches, where the acoustic part of the phonon specific heat can be described by the Debye model (eqn (6.3))

$$C_{ph,D} = \frac{9 \cdot R}{\omega_D^3} \cdot \int_0^{\omega_D} \frac{\omega^2 \cdot \left(\frac{\omega}{2 \cdot T}\right)}{\sin h^2\left(\frac{\omega}{2 \cdot T}\right)} d\omega \qquad (6.3)$$

with R being the gas constant and $\omega_D = \theta_D/T$.

Herein, the three acoustic branches are taken as one triply degenerated branch. In a similar way, the Einstein model describes the optical branches,

$$C_{ph,Ei} = c_i \cdot R \cdot \frac{\left(\frac{\theta_{Ei}}{2T}\right)^2}{\sin h^2\left(\frac{\theta_{Ei}}{2T}\right)}, \qquad (6.4)$$

with c_i referring to the degeneracy of the corresponding Einstein modes. The three acoustic and nine optical branches of the phonon dispersion of the $Ni_4Sb_{12-x}Sn_x$ framework are then represented by (12 times) one Debye and two Einstein functions $(27 \cdot f_E + 9 \cdot f_E)$ with $c_1 = 27$ and $c_2 = 9$. To additionally account for the filler atom in the icosahedral voids, a further

Einstein function was added to describe the increase of phonon modes, with $c_3 = 3 \cdot y$, where y represents the filling level. The heat capacity of the skutterudites follows then from

$$C_p = C_{p,el} + C_{ph,D} + \sum_{i=1}^{n=2,3} C_{ph,Ei} \qquad (6.5)$$

with the sum running over two or three Einstein modes. The least squares fittings obtained according to this model are presented as dashed lines in Fig. 16 and the extracted data for Einstein and Debye temperatures are also listed in Table 7.
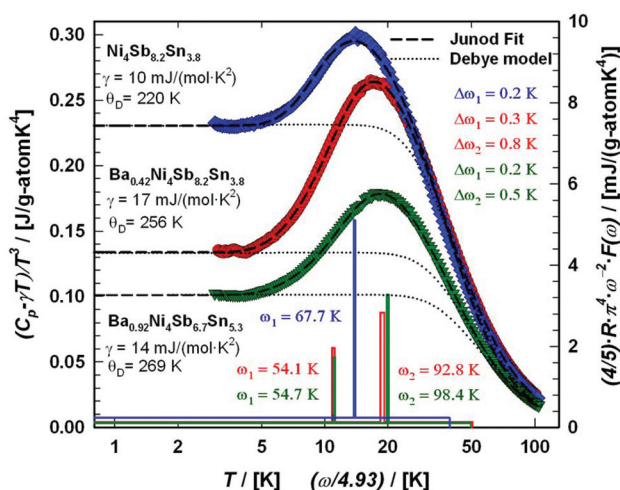
The second approach uses the model introduced by Junod et al.[57,58] to gain insight in the complex phonon spectrum. Special functionals of the phonon specific heat can take the form of convolutions of the phonon spectrum $F(\omega)$. Therefore, the electronic part of the specific heat is subtracted from $C_p(T)$ $(C_{ph}(T) = C_p(T) - \gamma \cdot T)$ and least squares fitting with two estimated Einstein-modes were applied to the phonon specific heat, as shown in Fig. 17, in the form of C_{ph}/T^3 vs. T. Further details on this method are described for example in ref. 59. In Fig. 17, the corresponding phonon spectra are plotted as solid lines scaled to the right axis. The simple Debye function based on eqn (6.3) is presented as a dotted line using the θ_D-data extracted together with the Sommerfeld coefficients. A comparison between filled and unfilled skutterudites shows that the filler element Ba has a strong influence on the Ni–Sn–Sb network. These results are also consistent with the increase in the Debye temperature. All data referring to the specific heat are listed in Table 7. The Debye and Einstein temperatures extracted by the two different methods described above match well with each other for all three samples investigated.

7. Electronic and thermal transport

As the $Ba_yNi_4Sb_{12-x}Sn_x$ compound exists within a wide homogeneity region, detailed investigations on the transport properties as a function of the composition were performed.

Electrical resistivity

Fig. 18a shows the temperature dependent electrical resistivities $\rho(T)$ of the unfilled single-phase skutterudite $Ni_4Sb_{8.2}Sn_{3.8}$ and the two Ba-filled skutterudites $Ba_{0.42}Ni_4Sb_{8.2}Sn_{3.8}$ and $Ba_{0.92}Ni_4Sb_{6.7}Sn_{5.3}$. These alloys show relatively low resistivities comparable to those of $Sn_yNi_4Sb_{12-x}Sn_x$ reported by Grytsiv et al.[18] While a decrease in the overall resistivity by filling $Ni_4Sb_{8.2}Sn_{3.8}$ with Ba atoms

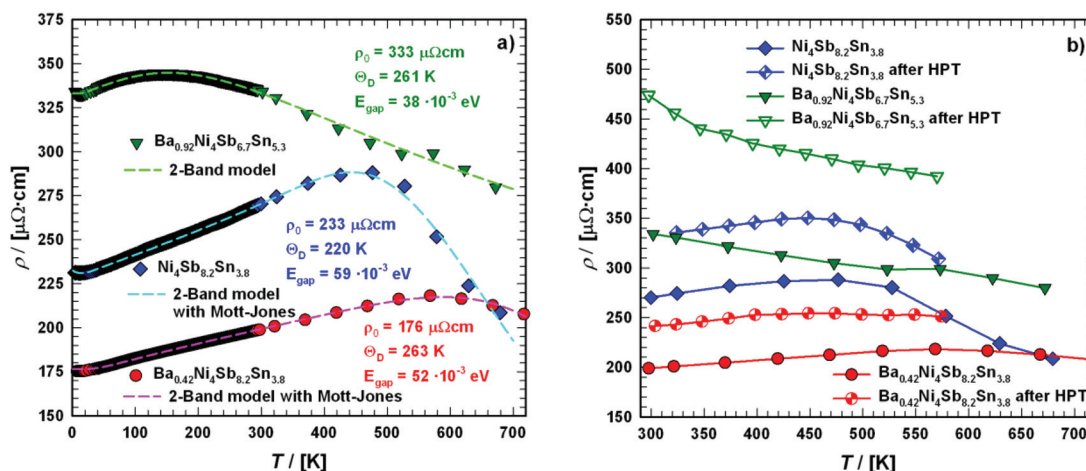**Fig. 17** Temperature-dependent specific heat of $Ni_4Sb_{8.2}Sn_{3.8}$, $Ba_{0.42}Ni_4Sb_{8.2}Sn_{3.8}$ and $Ba_{0.92}Ni_4Sb_{6.7}Sn_{5.3}$ plotted as $(C_p - \gamma \cdot T)/T^3$ versus $\ln(T)$. The least squares fitting was made to the experimental data using the model of Junod et al.[57,58] The blue, red and green lines (referring to the right axis) sketch the corresponding phonon spectral functions $F(\omega)$ plotted as $(4/5) \cdot R \cdot \pi^4 \cdot \omega^{-2} \cdot F(\omega)$ versus $\omega/4.93$ with ω in Kelvin. For comparison, a simple Debye model is added (dotted lines).

Fig. 18 Temperature-dependent electrical resistivities ρ of the skutterudites $Ni_4Sb_{8.2}Sn_{3.8}$, $Ba_{0.42}Ni_4Sb_{8.2}Sn_{3.8}$ and $Ba_{0.92}Ni_4Sb_{6.7}Sn_{5.3}$ (a) in the temperature range from 4 to 700 K and (b) when compared before and after SPD via HPT above room temperature. The dashed lines correspond to the least squares fitting according to a two-band model.

seems to correlate with an increase of the free carrier concentration, increasing the Sn-content seems to exert the inverse effect. Although the concept introduced by E. Zintl[60,61] is based on simple crystal chemistry, it appropriately describes the changes in $\rho(T)$ with the composition of $Ba_yNi_4Sb_{12-x}Sn_x$ alloys on the basis of a simple counting of charge carriers n_z, i.e.,

$$n_z = y \cdot 2(Ba) + 4 \cdot 10(Ni) - (12 - x) \cdot 3(Sb) - x \cdot 4(Sn) \quad (7.1)$$

This composition dependent change of carriers can also be seen from the Seebeck coefficients $S(T)$ of the three samples, as discussed below.

For all the three samples, the temperature dependent electrical resistivity exhibits two different regimes. At low temperatures, a metallic-like behaviour was obtained, which changes to a semiconducting behaviour at higher temperatures, at least up to 700 K. This change cannot be explained by a simple activation-type conductivity mechanism. Thus, a rectangular model for the density of states was considered (2-band model), with a narrow gap lying either slightly above or below the Fermi energy E_F,[62] which successfully described resistivities $\rho(T)$ of various clathrate and skutterudite systems (see for example ref. 18 and 59). While the former case describes holes as primary charge carriers, the latter one accounts for electrons as the dominating carriers. In these models, the unoccupied states above $E = E_F$ are available at $T = 0$ K. Simple metallic conductivity is possible at low temperatures but becomes semiconducting-like once electrons are excited across the energy gap of width E_{gap}. The total number of carriers (electrons and holes) is strongly dependent on the absolute temperature as well as on E_{gap}. On the basis of these assumptions, $\rho(T)$ can be calculated using

$$\rho(T) = \frac{\rho_0 \cdot n_0 + \rho_{ph}}{n(T)} \quad (7.2)$$

where n_0 gives the residual charge carrier density, $n(T)$ the total charge carrier density, ρ_0 is the residual resistivity and ρ_{ph} accounts for the scattering of electrons on the phonons, taking into account the Bloch Grüneisen law:

$$\rho(T) = \rho_0 + 4 \cdot \mathfrak{R} \cdot \theta_D \cdot \left(\frac{T}{\theta_D}\right)^5 \cdot \int_0^{\theta_D/T} \frac{x^5}{(e^x - 1) \cdot (1 - e^{-x})} \, dx + A \cdot T^3 \quad (7.3)$$

where $\mathfrak{R}$ stands for a temperature independent electron–phonon interaction constant and $A \cdot T^3$ represents the Mott–Jones term.[63] Least squares fitting according to eqn (7.2) was performed for $Ni_4Sb_{8.2}Sn_{3.8}$, $Ba_{0.42}Ni_4Sb_{8.2}Sn_{3.8}$ and $Ba_{0.92}Ni_4Sb_{6.7}Sn_{5.3}$ extracting ρ_0 and E_{gap}, which are listed in Table 8. The Debye temperatures θ_D are listed in Table 7 and can be compared to data obtained using other methods (see below).

Hall data

The Hall effect was studied for all three single-phase samples $Ni_4Sb_{8.2}Sn_{3.8}$, $Ba_{0.42}Ni_4Sb_{8.2}Sn_{3.8}$ and $Ba_{0.92}Ni_4Sb_{6.7}Sn_{5.3}$,

Table 8 Comparison of the physical properties for the filled and unfilled $Ba_yNi_4Sb_{12-x}Sn_x$ skutterudites

| Composition	Filling level	n_z	$n \times 10^{20}$ [cm^{-3}]	ρ_0 [$\mu\Omega$ cm]	E_{gap} [meV] [a,b]
$Ni_4Sb_{8.2}Sn_{3.8}$	0	0.2	2.13	233	59/53
$Ba_{0.42}Ni_4Sb_{8.2}Sn_{3.8}$	0.42	1.04	4.15	176	52/49
$Ba_{0.92}Ni_4Sb_{6.7}Sn_{5.3}$	0.92	0.54	4.63	333	38/36

[a] Gained from the fit of temperature dependent electrical resistivity.
[b] Gained from the minimum of the Seebeck coefficient.

revealing electrons as the predominant charge carriers. In Fig. 19, the charge carrier densities for the three samples as a function of temperature are displayed. For $Ni_4Sb_{8.2}Sn_{3.8}$ and $Ba_{0.42}Ni_4Sb_{8.2}Sn_{3.8}$, the charge carrier density does not change with temperature, which is a typical metallic-like behaviour. For $Ba_{0.92}Ni_4Sb_{6.7}Sn_{5.3}$, the early crossover from metallic to semi-conducting behaviour results in an increase of the charge carrier density with increasing temperature.

The charge carrier mobility μ for the three samples $Ni_4Sb_{8.2}Sn_{3.8}$, $Ba_{0.42}Ni_4Sb_{8.2}Sn_{3.8}$ and $Ba_{0.92}Ni_4Sb_{6.7}Sn_{5.3}$ is shown in Fig. 20. The mobility μ was calculated from the relation $\mu = \sigma/n \cdot e$, with σ being the electrical conductivity, n the charge carrier density and e the carrier charge (in this case electron charge). The temperature independent mobility $\mu(T)$ below 100 K was revealed from detailed analysis, i.e., assuming non-degeneracy for charge carriers and a distribution function given by Maxwell–Boltzmann statistics, usually attributed to neutral impurity scattering in semiconductors.[59] For $Ni_4Sb_{8.2}Sn_{3.8}$ and $Ba_{0.42}Ni_4Sb_{8.2}Sn_{3.8}$, the decrease in μ with temperature between 100 to 300 K was close to $T^{-1/2}$, which suggests alloy scattering as the main scattering process. This effect occurs whenever different atoms in the semiconductor
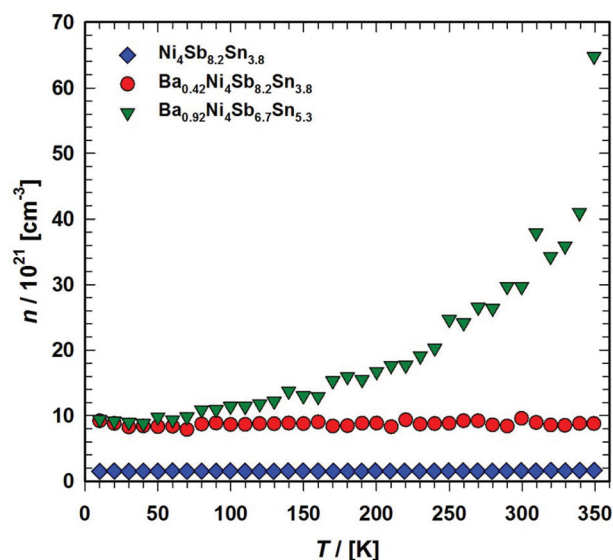
Fig. 19 Temperature dependent charge carrier densities n of the skutterudites $Ni_4Sb_{8.2}Sn_{3.8}$, $Ba_{0.42}Ni_4Sb_{8.2}Sn_{3.8}$ and $Ba_{0.92}Ni_4Sb_{6.7}Sn_{5.3}$.

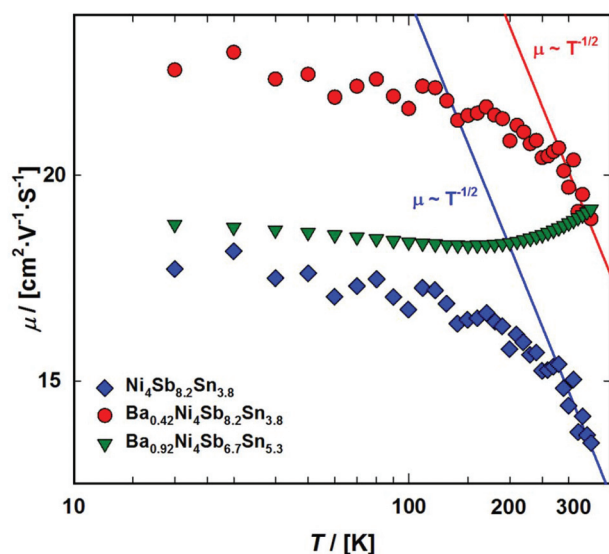**Fig. 20** Temperature dependent charge carrier mobilities μ of the skutterudites $Ni_4Sb_{8.2}Sn_{3.8}$, $Ba_{0.42}Ni_4Sb_{8.2}Sn_{3.8}$ and $Ba_{0.92}Ni_4Sb_{6.7}Sn_{5.3}$.

compounds are not arranged periodically in the crystal structure.[64]

The electron effective mass m^* can be calculated using eqn (7.4), which is usually valid for a single parabolic band at high n and/or low T.[65] Evaluation shows a significant increase in the effective mass with increasing filling level, rising from $3.7m_e$ for $Ni_4Sb_{8.2}Sn_{3.8}$ to $7.6m_e$ for $Ba_{0.42}Ni_4Sb_{8.2}Sn_{3.8}$. For $Ba_{0.92}Ni_4Sb_{6.7}Sn_{5.3}$, a further increase up to a value of $15.2m_e$ was found. In addition to the increase in mobility at higher temperature, this indicates that the assumption of a single parabolic band is not valid. The Pisarenko plot (Fig. 21) shows
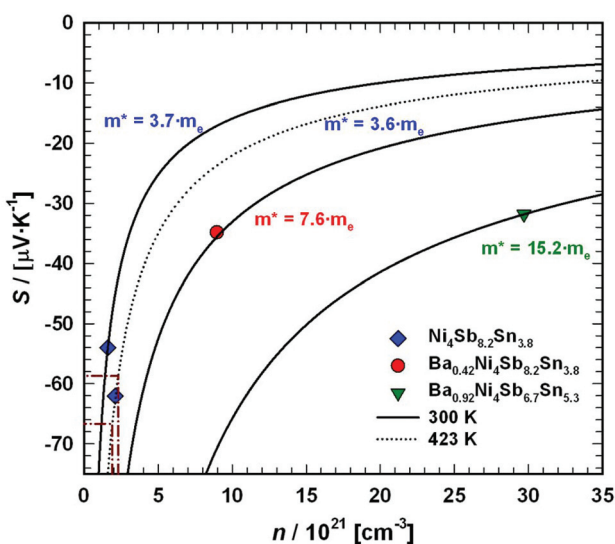

Fig. 21 Pisarenko plot showing the measured Seebeck coefficients at 300 K for the samples $Ni_4Sb_{8.2}Sn_{3.8}$, $Ba_{0.42}Ni_4Sb_{8.2}Sn_{3.8}$ and $Ba_{0.92}Ni_4Sb_{6.7}Sn_{5.3}$ as a function of the charge carrier density.

the Seebeck coefficients at 300 K as a function of charge carrier density. The dashed line indicates the maximum thermoelectric performance for the unfilled sample $Ni_4Sb_{8.2}Sn_{3.8}$ at 423 K.

Thermopower

The temperature-dependent Seebeck coefficients, $S(T)$, for the samples with the composition $Ni_4Sb_{8.2}Sn_{3.8}$, $Ba_{0.42}Ni_4Sb_{8.2}Sn_{3.8}$ and $Ba_{0.92}Ni_4Sb_{6.7}Sn_{5.3}$ are displayed in Fig. 22a. $S(T)$ is negative at low temperatures up to at least 400 K, suggesting that the transport phenomena are dominated by electrons as charge carriers, indicating n-type behaviour. This can be explained by the Zintl concept in parallel to the electrical resistivity, as discussed above. Below about 400 K, $S(T)$ behaves almost linearly before reaching a minimum between 400 and 500 K. The Seebeck coefficient can be understood in terms of Mott's formula:[65]

$$S(T > \theta_D) = \frac{2 \cdot \pi^2 \cdot k_B{}^2 \cdot m^*}{e \cdot \hbar^2 \cdot (3 \cdot n \cdot \pi^2)^{\frac{2}{3}}} \qquad (7.4)$$

with m^* being the effective mass and e the respective charge of the carriers involved. Eqn (7.4) is assumed to be valid for systems without significant electronic correlations.

Furthermore, Goldsmid and Sharp[66] showed the possibility for estimating the gap width E_{gap} from the maximum/minimum of $S(T)$, i.e.,

$$S_{max} = \frac{E_g}{2 \cdot e \cdot T_{max/min}} \qquad (7.5)$$

As in the present case, $S(T)$ is negative over the entire temperature range investigated, the minima data were inserted into eqn (7.5), leading to the results summarized in Table 8. The estimated gap energies E_{gap} are in accordance with those obtained from temperature dependent electrical resistivity and show a significant decrease from $Ba_{0.42}Ni_4Sb_{8.2}Sn_{3.8}$ to $Ba_{0.92}Ni_4Sb_{6.7}Sn_{5.3}$. A higher Sn content in the network (24g site) appears to influence the band structure more than an increased Ba filling level in the icosahedral voids (2a site).

Thermal conductivity

Fig. 23 presents the temperature-dependent thermal conductivities, $\kappa(T)$, of the three compounds: $Ni_4Sb_{8.2}Sn_{3.8}$, $Ba_{0.42}Ni_4Sb_{8.2}Sn_{3.8}$ and $Ba_{0.92}Ni_4Sb_{6.7}Sn_{5.3}$.

Radiation losses in the low-temperature steady-state heat flow measurements were corrected subtracting a Stefan–Boltzmann $A \cdot T^3$ term. In general, the thermal conductivities are quite high when compared with those of other skutterudites (see for example ref. 8–11), but they lie in the same range as those obtained by Grytsiv et al.[18] for their Sn filled and unfilled $Sn_yNi_4Sb_{12-x}Sn_x$ compounds. For a more detailed analysis (shown in Fig. 25), only data between 4 and 300 K were taken into account. The total thermal conductivity can be written as

$$\kappa = \kappa_{el} + \kappa_{ph} \qquad (7.6)$$

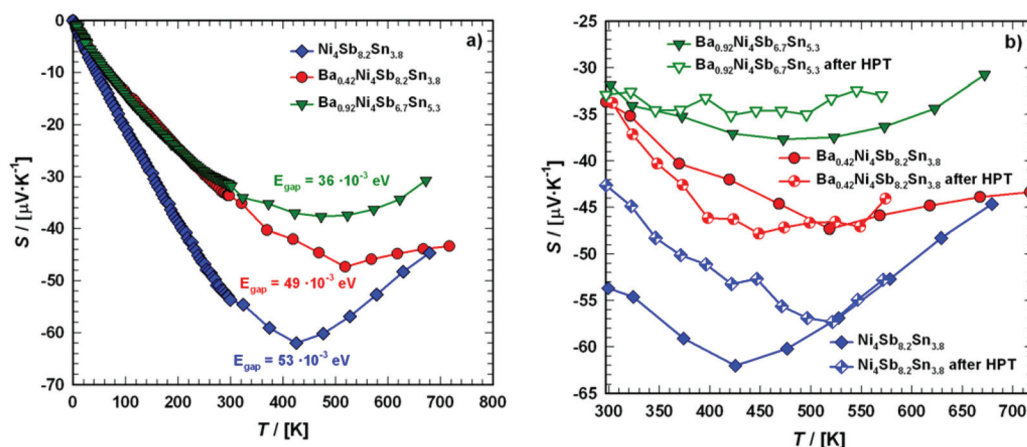**Fig. 22** Temperature dependent Seebeck coefficient S of the skutterudites $Ni_4Sb_{8.2}Sn_{3.8}$, $Ba_{0.42}Ni_4Sb_{8.2}Sn_{3.8}$ and $Ba_{0.92}Ni_4Sb_{6.7}Sn_{5.3}$ (a) in the temperature range from 4 to 700 K and (b) when compared before and after HPT above room temperature.
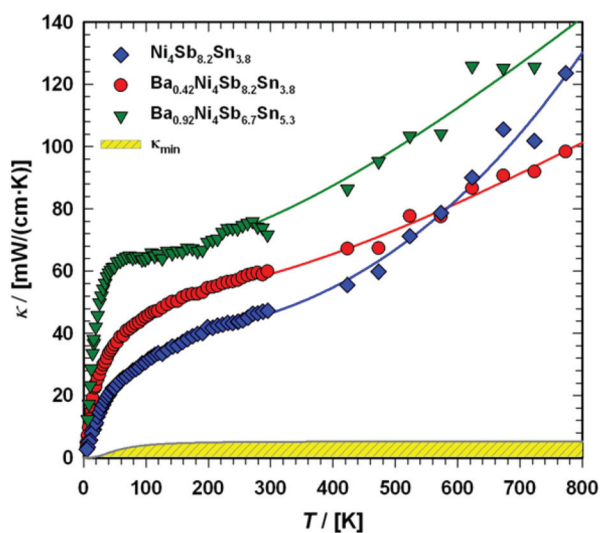

Fig. 23 Temperature dependent thermal conductivity κ of the skutterudites $Ni_4Sb_{8.2}Sn_{3.8}$, $Ba_{0.42}Ni_4Sb_{8.2}Sn_{3.8}$ and $Ba_{0.92}Ni_4Sb_{6.7}Sn_{5.3}$. The shaded area represents the minimum thermal conductivity κ_{min}. The solid lines are guides for the eye.

where κ_{el} presents the electronic part and κ_{ph} the phonon part. A number of scattering processes limits both contributions, so that a finite thermal conductivity will result in any case. For simple metals, κ_{el} can be calculated from the temperature dependent electrical resistivity *via* the Wiedemann Franz law:

$$\kappa_{el} = \frac{L_0(T)\cdot T}{\rho(T)}, \tag{7.7}$$

where the temperature dependent Lorentz number $L_0(T)$ is given by

$$L_0(T) = \left(\frac{k_B}{e}\right)^2 \cdot \left[\frac{(s+7/2)\cdot F_{s+5/2}(\xi)}{(s+3/2)\cdot F_{s+1/2}(\xi)} - \left(\frac{(s+5/2)\cdot F_{s+3/2}(\xi)}{(s+3/2)\cdot F_{s-1/2}(\xi)}\right)^2\right] \tag{7.8}$$

as proposed by Rowe *et al.*[67]

In order to obtain the correct values for $L_0(T)$, the reduced Fermi energy,
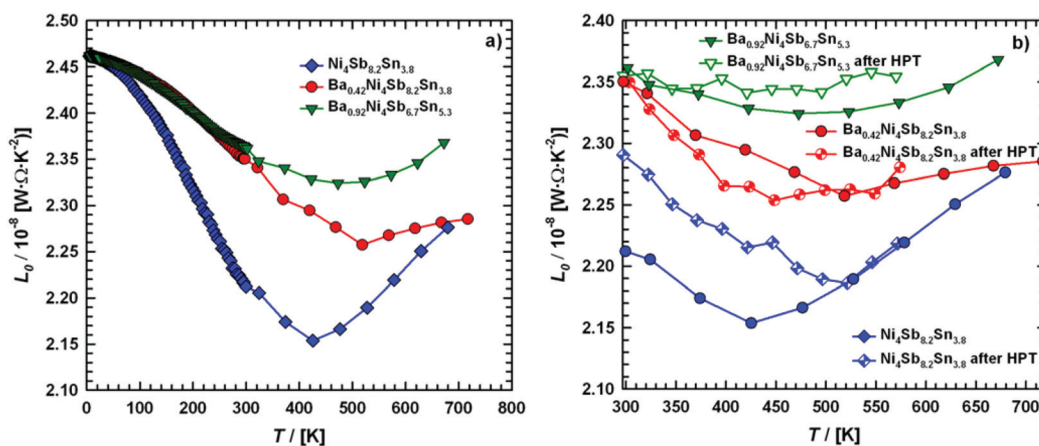
$$\xi = \frac{E_F}{k_B\cdot T}, \tag{7.9}$$

Fig. 24 (a) Temperature dependent Lorentz number L_0 of the skutterudites $Ni_4Sb_{8.2}Sn_{3.8}$, $Ba_{0.42}Ni_4Sb_{8.2}Sn_{3.8}$ and $Ba_{0.92}Ni_4Sb_{6.7}Sn_{5.3}$, and (b) a comparison before and after HPT above room temperature.

has to be extracted from the measured Seebeck coefficients and $F_n(\xi)$ being the nth order Fermi integral, according to

$$S = \pm \frac{k_B}{e} \cdot \left[\frac{(s+5/2) \cdot F_{s+3/2}(\xi)}{(s+3/2) \cdot F_{s-1/2}(\xi)} - \xi \right], \qquad (7.10)$$

$$F_n(\xi) = \int_0^\infty \frac{x^n}{1+e^x} dx, \qquad (7.11)$$

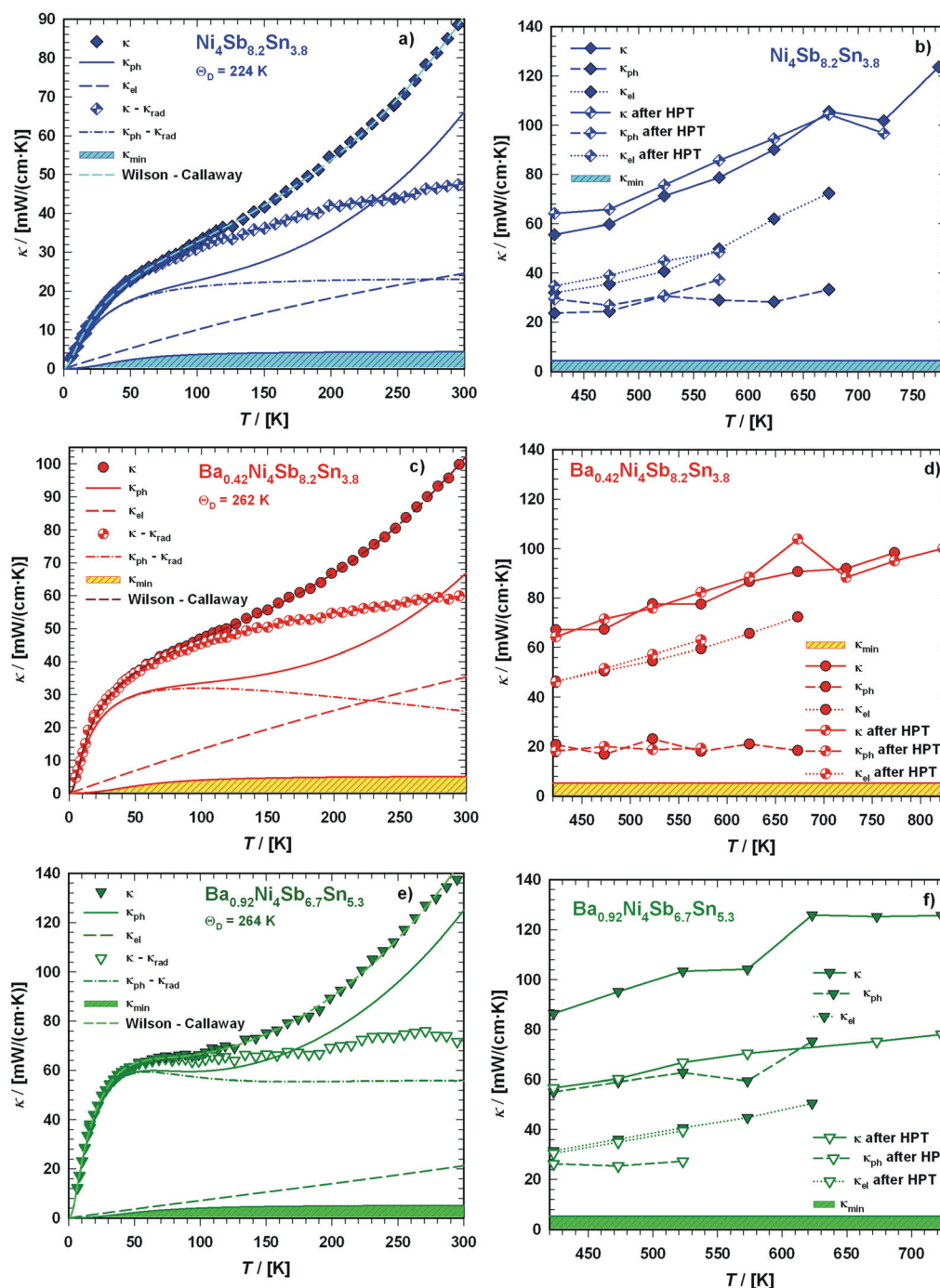**Fig. 25** Temperature dependent thermal conductivity κ of the skutterudites $Ni_4Sb_{8.2}Sn_{3.8}$, $Ba_{0.42}Ni_4Sb_{8.2}Sn_{3.8}$ and $Ba_{0.92}Ni_4Sb_{6.7}Sn_{5.3}$ at low temperatures ((a), (c), (e)) and above room temperature ((b), (d), (f)) with a comparison to the values measured after HPT. The dashed lines are least squares fits according to a combination of the Wilson and Callaway models.

with k_B being the Boltzmann constant, e the electron charge, E_F the Fermi energy and s the scattering parameter. Assuming acoustic phonon scattering as the main carrier scattering mechanism, $s = -1/2$, $L_0(T)$ can be calculated by substituting s and ξ in eqn (7.8). The calculated values for the three compounds, $Ni_4Sb_{8.2}Sn_{3.8}$, $Ba_{0.42}Ni_4Sb_{8.2}Sn_{3.8}$ and $Ba_{0.92}Ni_4Sb_{6.7}Sn_{5.3}$ are shown in Fig. 24, ranging from 2.15 to 2.46 W Ω K^{-2}.

Subtracting the κ_{el} term from the measurement data results in κ_{ph}, as shown in Fig. 25a, c and e. For all three samples, the electronic part is quite low but is enhanced at higher temperature. According to the Matthiessen rule, the electronic thermal resistivity, W_{el} of a simple metal can be written in terms of the thermal resistivity, $W_{el,0}$ caused by electron scattering due to impurities and defects as well as that caused by electrons scattered due to thermally excited phonons, $W_{el,ph}$:

$$W_{el} \equiv \frac{1}{\kappa_{el}} = W_{el,0} + W_{el,ph}. \qquad (7.12)$$

Using the Wilson equation,[68] $W_{el,ph}$ can be expressed as

$$W_{el,ph} = \frac{A}{L_0 \cdot T} \cdot \left(\frac{T}{\theta_D}\right)^5 \cdot J_5\left(\frac{\theta_D}{T}\right) \cdot \left[1 + \frac{3}{\pi^2} \cdot \left(\frac{k_F}{q_D}\right)^2 \cdot \left(\frac{\theta_D}{T}\right)^2 - \frac{1}{2 \cdot \pi^2} \cdot \frac{J_7(\theta_D/T)}{J_5(\theta_D/T)}\right] \qquad (7.13)$$

with k_F being the wave vector at the Fermi surface, q_D the phonon Debye wave vector and A a material constant, which depends on the strength of the electron–phonon interaction, Debye temperature, the effective mass of an electron, the number of unit cells per unit volume, Fermi velocity and the electron wavenumber at the Fermi surface. The integrals J_n have the form,

$$J_n(x) = \int_0^x \frac{z^n}{(e^z - 1) \cdot (1 - e^{-z})} dz \qquad (7.14)$$

with $z = \frac{\theta_D}{T}$. In non-metallic systems, the lattice thermal conductivity is the dominant part of the thermal conduction mechanism, which can be described by a model introduced by Callaway.[69–71] Accordingly, heat carrying lattice vibrations can be described by

$$\kappa_{ph} = \frac{k_B}{2 \cdot \pi^2 \cdot v_s} \cdot \left(\frac{k_B}{\hbar}\right)^3 \cdot T^3 \cdot \int \frac{\tau_c \cdot x^4 \cdot e^x}{(e^x - 1)^2} dx + I_2 \qquad (7.15)$$

with the velocity of sound as derived within the Debye model:

$$v_s = \frac{k_B \cdot \theta_D}{\hbar \cdot (6 \cdot \pi^2 \cdot N)^{1/3}} \qquad (7.16)$$

and

$$x = \frac{\hbar \cdot \omega}{k_B \cdot T} \qquad (7.17)$$

where N is the number of atoms per unit volume and ω the phonon frequency.

The second integral I_2 in eqn (7.15) can be expressed as

$$I_2 = \left[\int_0^{\theta_D/T} \frac{\tau_c}{\tau_N} \cdot \frac{x^4 \cdot e^x}{(e^x - 1)^2} dx\right] / \int \frac{1}{\tau_N} \cdot \left(1 - \frac{\tau_c}{\tau_N}\right) \cdot \frac{x^4 \cdot e^x}{(e^x - 1)^2} dx \qquad (7.18)$$

where

$$\tau_c^{-1} = \tau_N^{-1} + \tau_D^{-1} + \tau_U^{-1} + \tau_B^{-1} + \tau_E^{-1}. \qquad (7.19)$$

Here, τ_N^{-1}, τ_D^{-1}, τ_U^{-1}, τ_B^{-1} and τ_E^{-1} denote the normal 3-phonon scattering process, scattering by low-dimensional lattice defects, Umklapp processes, boundary scattering and scattering of phonons by electrons, respectively.

The dashed lines in Fig. 25a, c and e refer to least squares fitting according to eqn (7.6) assuming a combination of the Wilson and Callaway models for κ_{el} and κ_{ph}. The extracted values for the Debye temperatures θ_D are listed in Table 7 and show a good agreement with the values gained from various other methods described in this article and compare well with literature data.

The minimum thermal conductivity κ_{min}, presented as shaded area in Fig. 25a, c and e, was estimated by the model of Cahill and Pohl:[72,73]

$$\kappa_{min} = \left(\frac{3 \cdot N}{4 \cdot \pi}\right)^{\frac{1}{3}} \cdot \frac{k_B^2 \cdot T^2}{\hbar \cdot \theta_D} \cdot \int_0^{\theta_D/T} \frac{x^3 \cdot e^x}{(e^x - 1)^2} dx. \qquad (7.20)$$

Here, N is the number of atoms per unit volume and x is a dimensionless parameter connected to the phonon frequency ω via $x = \frac{\hbar \cdot \omega}{k_B \cdot T}$. Fig. 25b, d and f compare the situation for temperatures above 300 K. For the two compounds, $Ni_4Sb_{8.2}Sn_{3.8}$ and $Ba_{0.42}Ni_4Sb_{8.2}Sn_{3.8}$, κ_{el} is the dominant part of thermal conductivity, whereas κ_{ph} is of the order of κ_{min}. For $Ba_{0.92}Ni_4Sb_{6.7}Sn_{5.3}$, both the parts, κ_{ph} as well as κ_{el}, are in the same order in magnitude but 2 to 3 times higher than those found for the previous samples. This may be caused by two effects: (i) substitution of Sb with Sn-atoms in the 24g site is combined with an increase in the thermal conductivity, or more likely, as reported in various articles,[74,75] (ii) the vibrations of the filler atom are not independent from those of the network atoms.

Figure of merit

The dimensionless figure of merit zT characterizes the thermoelectric ability of a single material concerning power generation or cooling. For commercial applications, a zT above 1 is desirable. The temperature dependent figure of merit can be calculated using eqn (1.1) and is shown in Fig. 26a. Although the electrical resistivity for all the three investigated compounds $Ni_4Sb_{8.2}Sn_{3.8}$, $Ba_{0.42}Ni_4Sb_{8.2}Sn_{3.8}$ and $Ba_{0.92}Ni_4Sb_{6.7}Sn_{5.3}$ is quite low, low absolute values of the Seebeck coefficients $S(T)$ (<70 µV K^{-1}) and high thermal conductivities $\kappa(T)$ (>20 mW cm^{-1} K^{-1}) prevent zT from reaching values above 0.11 at RT. As already could be seen from the Pisarenko plot, the highest values for zT are achieved from the unfilled sample $Ni_4Sb_{8.2}Sn_{3.8}$.
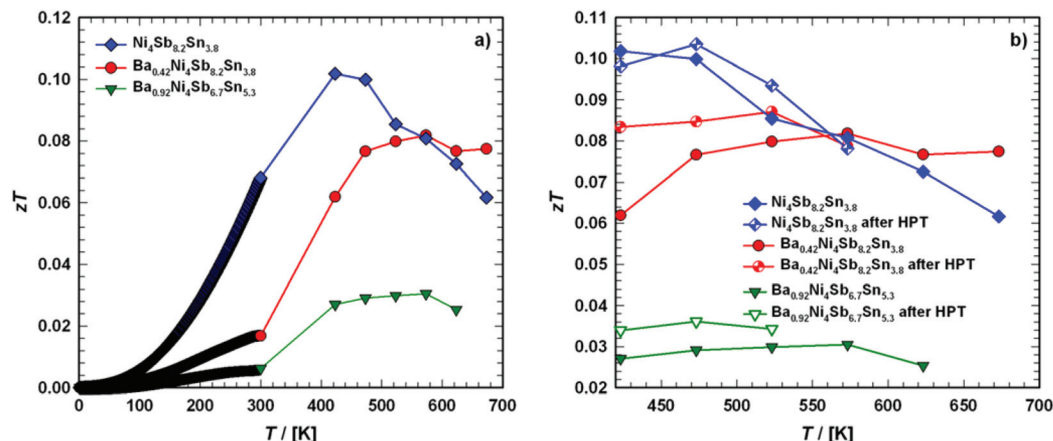
Fig. 26 Temperature dependent figure of merit zT for the skutterudites $Ni_4Sb_{8.2}Sn_{3.8}$, $Ba_{0.42}Ni_4Sb_{8.2}Sn_{3.8}$ and $Ba_{0.92}Ni_4Sb_{6.7}Sn_{5.3}$ (a) in the temperature range from 4 to 700 K and (b) when compared before and after HPT above room temperature.

8. Transport properties after high-pressure torsion (HPT)

Severe plastic deformation (SPD) *via* HPT is one technique to significantly increase the performance of thermoelectric materials,[76–78] with various effects being responsible for this behaviour. Because of the interdependence of ρ, S and κ_{el}, one strategy to increase zT is to reduce the κ_{ph} by increasing the scattering of heat carrying phonons *via* various mechanisms, as already discussed in chapter 7 in terms of their corresponding relaxation times τ_n (eqn (7.19)). In general, I_2 in eqn (7.18) is negligible for $\tau_N \gg \tau_U$. A possible route to decrease κ_{ph} therefore is either to reduce the grain size d_g, because $\tau_B^{-1} = v_s/d_g$, and to increase the density of dislocations, as τ_D^{-1} includes the contribution of dislocations. This term consists of the dislocation core,

$$\tau_{core}^{-1} \propto \frac{N_D \cdot r^4 \cdot \omega^3}{v_c} \tag{8.1}$$

with N_D being the dislocation density, and of the dislocation strain field,

$$\tau_{str}^{-1} \propto \frac{N_D^2 \cdot b \cdot \omega}{2 \cdot \pi}. \tag{8.2}$$

Here b represents the Burgers vector of the dislocation. Hence, a smaller grain size and/or higher dislocation density results in enhanced phonon scattering on both electrons as well as on lattice defects and this way decreases κ_{ph}. Furthermore, Hicks and Dresselhaus[79,80] demonstrated that grain sizes, approaching nanometer length scales (favourable <10 nm) are able to influence the Seebeck coefficient. On inspecting Mott's formula (eqn (7.4)), it can be seen that the Seebeck coefficient is primarily dependent on the logarithmic energy derivative of the electronic density of states (DOS) at the Fermi-energy. Therefore, any method that is able to increase the slope at E_F for a given number of states N will increase S. HPT uses this concept by the transition from a parabolic elec-

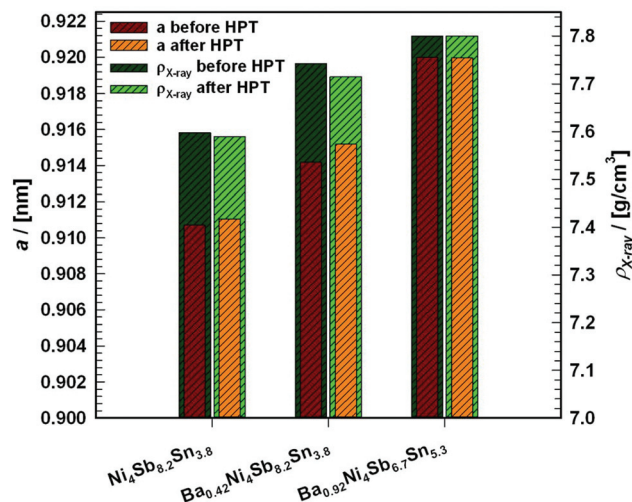**Fig. 27** Comparison of the lattice parameters a and corresponding X-ray densities ρ_{X-ray} of the skutterudites $Ni_4Sb_{82}Sn_{3.8}$, $Ba_{0.42}Ni_4Sb_{8.2}Sn_{3.8}$ and $Ba_{0.92}Ni_4Sb_{6.7}Sn_{5.3}$ before and after SPD *via* HPT.

tronic DOS curve to a spike-like curve while going from macroscopic bulk structures to nanosized ones. With these observations, a way is opened to influence S independently from ρ and κ_{el}. Based on this knowledge, HPT was performed by applying a hydrostatic pressure of 4 GPa, one revolution and a processing temperature of 400 °C on two skutterudite samples, $Ni_4Sb_{8.2}Sn_{3.8}$ and $Ba_{0.42}Ni_4Sb_{8.2}Sn_{3.8}$, whereas for compound $Ba_{0.92}Ni_4Sb_{6.7}Sn_{5.3}$, a temperature of 300 °C was used. During the deformation, the sample's geometry remains constant and the application of enhanced hydrostatic pressure enables practically unlimited plastic strain without early failure and crack formation.[81,82] Therefore, with the hydrostatic pressure not only low dimensional defects are created, but also grain boundaries are built up from these defects.[82–87] The resulting shear strain corresponds to eqn (2.4); thus, the deformation affects the samples rim more than the centre.

Therefore, the physical properties of the processed specimens always cover the more and less deformed parts. Pieces of all parts of the HPT processed samples were collected and used for X-ray powder analysis. In general, an increase in the half width of the X-ray patterns as well as of the lattice parameters was observed, indicating a reduction of the crystallite size and an increase of the dislocation density. For the $Ni_4Sb_{8.2}Sn_{3.8}$ and $Ba_{0.42}Ni_4Sb_{8.2}Sn_{3.8}$ samples, this behaviour is distinct, whereas for compound $Ba_{0.92}Ni_4Sb_{6.7}Sn_{5.3}$, almost no change was visible (Fig. 27). The X-ray peak profile analysis shows a reduction in the grain size for all three samples (Fig. 28),
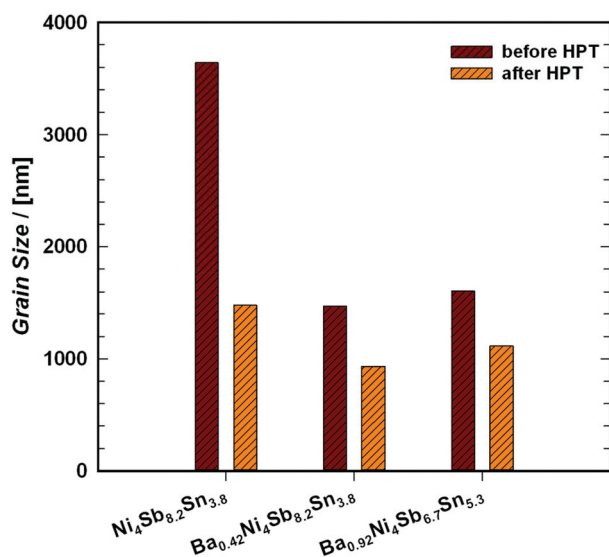
whereas the largest effect was observed for the unfilled sample $Ni_4Sb_{8.2}Sn_{3.8}$ (Fig. 28). In the EPMA micrographs before and after HPT (Fig. 29), no changes in the microstructure were observed. Due to microcracks, the density of the materials after HPT processing was lower than before (compare values given in Table 3 and Table 9). Fig. 18b, 22b, 24b, 25b, d and f summarize the effect of HPT treatment on the physical properties, $\rho(T)$, $S(T)$ and $\kappa(T)$.

The electrical resistivity for all the samples (Fig. 18b) after HPT was higher. While a crossover from metallic to semi-conducting behaviour was observed for $Ni_4Sb_{8.2}Sn_{3.8}$ and $Ba_{0.42}Ni_4Sb_{8.2}Sn_{3.8}$, $Ba_{0.92}Ni_4Sb_{6.7}Sn_{5.3}$ was semiconducting over the entire temperature range investigated. The data for the Seebeck coefficients after HPT (Fig. 22b) stay in the same range as those before HPT or are even slightly lower, which results in no evident change in the temperature dependent Lorentz number $L_0(T)$ (Fig. 24b). The thermal conductivity of the Sb-rich samples (Fig. 25b and d) seems to stay almost the same. Determining κ_{el} and κ_{ph} as shown in chapter 5 reveals that neither κ_{el} nor κ_{ph} was influenced significantly, resulting in no-evident change in the thermal conductivity κ. For the Sn-rich sample (Fig. 25f), both components, κ_{el} as well as κ_{ph}, are lowered leading to a decrease in the overall thermal conductivity κ. In contrast to the filled skutterudites without Sb–Sn substitution, all these observations show no significant

Fig. 28 Comparison of the grain sizes of the skutterudites $Ni_4Sb_{8.2}Sn_{3.8}$, $Ba_{0.42}Ni_4Sb_{8.2}Sn_{3.8}$ and $Ba_{0.92}Ni_4Sb_{6.7}Sn_{5.3}$ before and after SPD *via* HPT.

Table 9 Lattice parameters a and corresponding densities for the investigated $Ba_yNi_4Sb_{12-x}Sn_x$ skutterudites after HPT

Composition	a [nm]	ρ_X [g cm^{-3}]	ρ_s [g cm^{-3}]
$Ni_4Sb_{8.2}Sn_{3.8}$	0.91103(2)	7.589	7.437
$Ba_{0.42}Ni_4Sb_{8.2}Sn_{3.8}$	0.91518(8)	7.715	7.026
$Ba_{0.92}Ni_4Sb_{6.7}Sn_{5.3}$	0.91998(3)	7.801	7.414
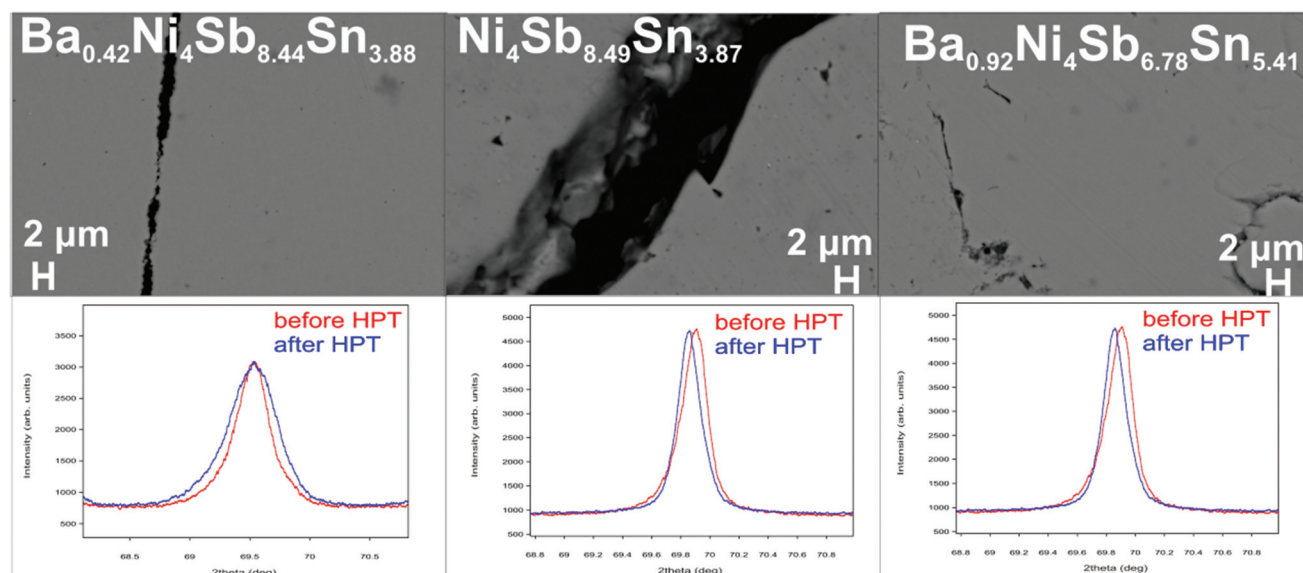
Fig. 29 Microstructure and X-ray profiles of the skutterudite samples $Ni_4Sb_{8.2}Sn_{3.8}$, $Ba_{0.42}Ni_4Sb_{8.2}Sn_{3.8}$ and $Ba_{0.92}Ni_4Sb_{6.7}Sn_{5.3}$ after HPT.

change in the figure of merit above room temperature (Fig. 26).

9. Thermal expansion

Fig. 30 shows the thermal expansion ($\Delta l/l_0$) for all the three single-phase samples, $Ni_4Sb_{8.2}Sn_{3.8}$, $Ba_{0.42}Ni_4Sb_{8.2}Sn_{3.8}$ and $Ba_{0.92}Ni_4Sb_{6.7}Sn_{5.3}$, measured with a capacitance dilatometer in the temperature range of 4.2–300 K. $\Delta l/l_0$ decreases almost linearly within the temperature range from room temperature to about 150 K, whereas for temperatures below 150 K, non-linear behaviour was observed. The data gained from the measurements using a dynamic mechanical analyser with the sample first cooled with liquid nitrogen and afterwards heated up or simply heated from room temperature to 400 K show a linear increase with increasing temperature (Fig. 31). The temperature derivative of the length change defines the thermal expansion coefficient α, *i.e.*

$$\alpha = \left(\frac{\partial \Delta l}{\partial l}\right) \cdot \frac{1}{l_0}. \tag{9.1}$$

Applying this model, α was calculated in the temperature range above 150 K up to 300 K (see dashed lines in the insert of Fig. 30) and also from a combination of the low and high temperature measurement data. The corresponding thermal expansion coefficients are listed in Table 7. The values obtained for the current samples lead to a good agreement between the high and low temperature data proven by the combination of the data according to Fig. 31. From Table 7, it follows that the thermal expansion coefficients α for $Ba_yNi_4Sb_{12-x}Sn_x$ based skutterudites lie within the range
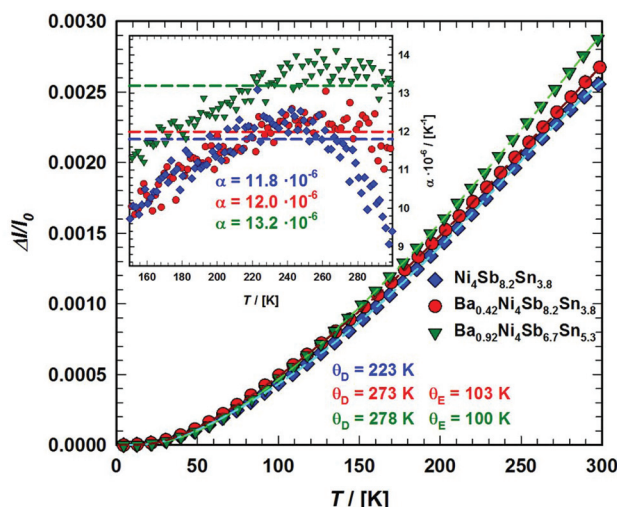

Fig. 30 Temperature dependent thermal expansion $\Delta l/l_0$ of the skutterudites $Ni_4Sb_{8.2}Sn_{3.8}$, $Ba_{0.42}Ni_4Sb_{8.2}Sn_{3.8}$ and $Ba_{0.92}Ni_4Sb_{6.7}Sn_{5.3}$ in the temperature range from 4.2 to 300 K. The inset shows the temperature dependence of α, whereas the dashed lines give the values obtained from the slope of the $\Delta l/l_0$ vs. T plot in their linear regions at higher temperatures.
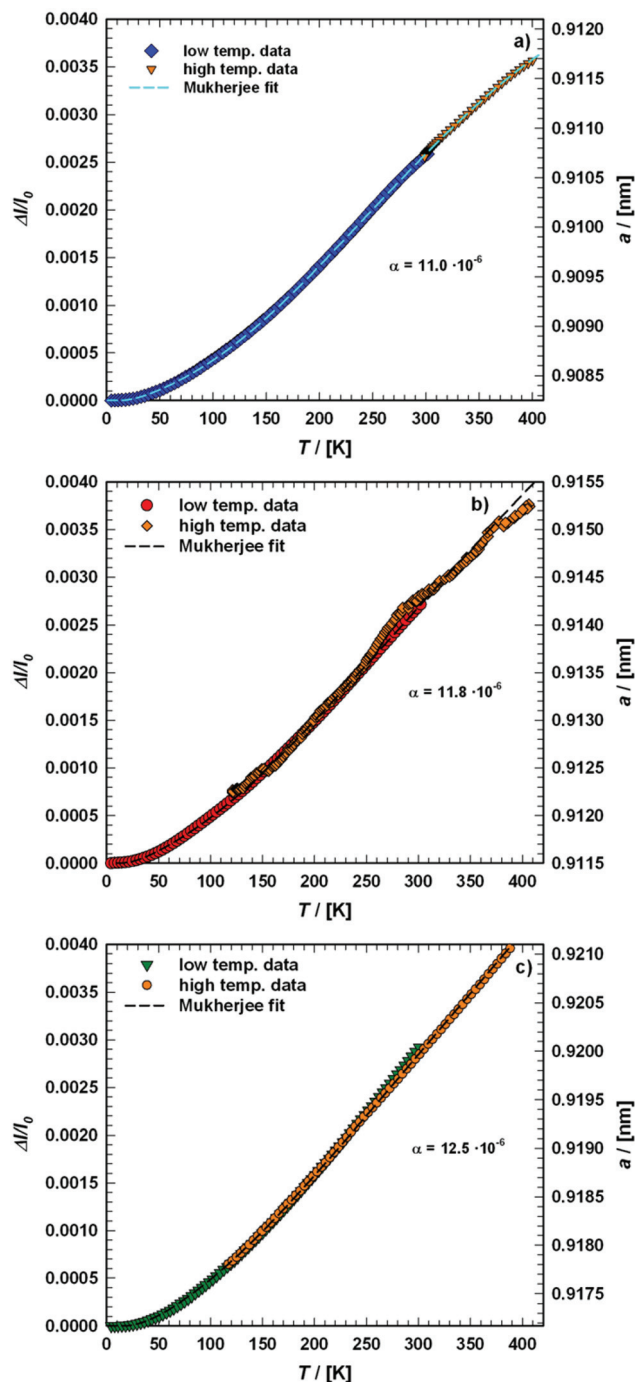

Fig. 31 Combination of the low and high temperature thermal expansion $\Delta l/l_0$ data for the skutterudites (a) $Ni_4Sb_{8.2}Sn_{3.8}$, (b) $Ba_{0.42}Ni_4Sb_{8.2}Sn_{3.8}$ and (c) $Ba_{0.92}Ni_4Sb_{6.7}Sn_{5.3}$. The dashed lines correspond to the least squares fits according to eqn (9.3).

obtained for other skutterudites.[22] A higher value of α occurs with a higher Ba filling level, visible at higher temperatures, which can be associated with the rattling behaviour of Ba on the 2a site inside the structural cage. For a cubic material, the lattice parameter varies with the temperature in parallel to the thermal expansion coefficient. Therefore, the lattice para-

meters a_n at various temperatures can be derived if a_n at a certain temperature is known, by applying eqn (9.2).

$$\alpha = \frac{a_2 - a_1}{a_1} / \Delta T. \tag{9.2}$$

The values according to all three specimens were added to Fig. 31. The higher Ba filling level results in larger lattice parameters for $Ba_{0.42}Ni_4Sb_{8.2}Sn_{3.8}$ and $Ba_{0.92}Ni_4Sb_{6.7}Sn_{5.3}$ when compared to $Ni_4Sb_{8.2}Sn_{3.8}$. To analyse the thermal expansion as a function of temperature over the entire temperature range from 4.2 to 400 K, a semi-classical model, introduced by Mukherjee[88] was used. This model takes into account three- and four-phonon interactions, considering anharmonic potentials and uses both the Debye model for the acoustic phonons and the Einstein model for the optical modes. The length change $\Delta l / l(T_0)$ is then given by

$$\frac{\Delta l}{l(T_0)} = \frac{\langle x \rangle_T - \langle x \rangle_{T_0}}{x_0} \tag{9.3}$$

with

$$\langle x \rangle_T = \frac{\xi}{2} \cdot T^2 + \frac{3 \cdot g}{4 \cdot c^2} \cdot (\varepsilon - G \cdot \varepsilon^2 - F \cdot \varepsilon^3) \tag{9.4}$$

and ε of the form,

$$\varepsilon = \left\{ \left(\frac{3}{p}\right) \cdot 3 \cdot k_B \cdot T \cdot \left(\frac{T}{\theta_D}\right)^3 \cdot \int \frac{z^3}{e^z - 1} \, dz + \left(\frac{p-3}{p}\right) \cdot \frac{k_B \cdot \theta_E}{e^{\theta_D/T} - 1} \right\} \tag{9.5}$$

Herein, ξ stands for the electronic contribution to the average lattice displacement, θ_D is the Debye temperature, θ_E is the Einstein temperature and p is the average number of phonon branches actually exited over the temperature range with G, F, c, and g being material constants. Least squares fitting to the experimental data according to eqn (9.3) were added to Fig. 30 and 31 as dashed lines. The values obtained for θ_D and θ_E are listed in Table 7 and can be compared with the data gained from fitting to the electrical resistivity, thermal conductivity and specific heat. This comparison shows good agreement among data from the various methods as well as with those available in the literature.

10. Elastic properties

As the average symmetry of skutterudites is isotropic, the Young's modulus E and Poisson's ratio ν can be gained by fitting the variables of the materials eigenfrequencies obtained from the RUS measurements of all three single-phase samples

$Ni_4Sb_{8.2}Sn_{3.8}$, $Ba_{0.42}Ni_4Sb_{8.2}Sn_{3.8}$ and $Ba_{0.92}Ni_4Sb_{6.7}Sn_{5.3}$. Based on these data, all other elastic properties were calculated. The shear modulus G and the bulk modulus B can be obtained from

$$G = \frac{E}{2 \cdot (\nu + 1)} \tag{10.1}$$

and

$$B = \frac{E}{3 \cdot (1 - 2 \cdot \nu)}. \tag{10.2}$$

For an isotropic material, the elastic constant C_{11} is given by

$$C_{11} = 3 \cdot B - \frac{6 \cdot B \cdot \nu}{1 + \nu}. \tag{10.3}$$

The longitudinal (ν_L) and the transversal (ν_T) sound velocities can be derived from one of the following relations:

$$C_{44} = G = \rho_s \cdot \nu_T{}^2 \tag{10.4}$$

$$C_{11} = \rho_s \cdot \nu_L{}^2 \tag{10.5}$$

Herein, ρ_s is the samples' density measured *via* Archimedes' principle. From the knowledge of ν_L and ν_T, the materials mean sound velocity ν_m can be calculated using eqn (10.6).

$$\nu_m = \left[\frac{1}{3} \cdot \left(\frac{2}{\nu_T{}^3} + \frac{1}{\nu_L{}^3} \right) \right]^{-1/3} \tag{10.6}$$

Anderson's relation[89] yields the Debye temperature θ_D from the elastic properties measurements.

$$\theta_D = \frac{h}{k_B} \cdot \left(\frac{3 \cdot n_{ASU} \cdot N_A \cdot \rho_s}{4 \cdot M \cdot \pi} \right)^{1/3} \cdot \nu_m. \tag{10.7}$$

In eqn (10.7), h denotes Plank's constant, k_B is the Boltzmann constant, N_A is Avogadro's number, M is the molecular weight and n_{ASU} stands for the number of atoms in the asymmetric unit. The data extracted for compounds $Ni_4Sb_{8.2}Sn_{3.8}$, $Ba_{0.42}Ni_4Sb_{8.2}Sn_{3.8}$ and $Ba_{0.92}Ni_4Sb_{6.7}Sn_{5.3}$ are listed in Table 10 and are shown in Fig. 32. A comparison with the elastic property data available in the literature (see for example ref. 23) shows that $Ba_yNi_4Sb_{12-x}Sn_x$ based skutterudites are characterized by a rather low Young's modulus and high Poisson's ratio, continuing this trend for the bulk modulus, longitudinal (ν_L), transversal (ν_T) and mean sound velocity. The extracted Debye temperatures (see Table 7) lie in the same range as the values gathered using other methods, as listed in the previous chapters.

Table 10 Elastic properties of the $Ba_yNi_4Sb_{12-x}Sn_x$ skutterudites investigated

Composition	ν	E [GPa]	G [GPa]	B [GPa]	C_{11} [GPa]	C_{44} [GPa]	$\nu_L \times 10^5$ [cm s^{-1}]	$\nu_T \times 10^5$ [cm s^{-1}]	$\nu_m \times 10^5$ [cm s^{-1}]
$Ni_4Sb_{8.2}Sn_{3.8}$	0.274	100.49	39.44	74.11	126.69	39.44	4.11	2.29	2.55
$Ba_{0.42}Ni_4Sb_{8.2}Sn_{3.8}$	0.262	108.00	42.79	75.63	132.68	42.79	4.19	2.38	2.64
$Ba_{0.92}Ni_4Sb_{6.7}Sn_{5.3}$	0.273	115.8	45.48	85.02	145.67	45.48	4.35	2.43	2.71
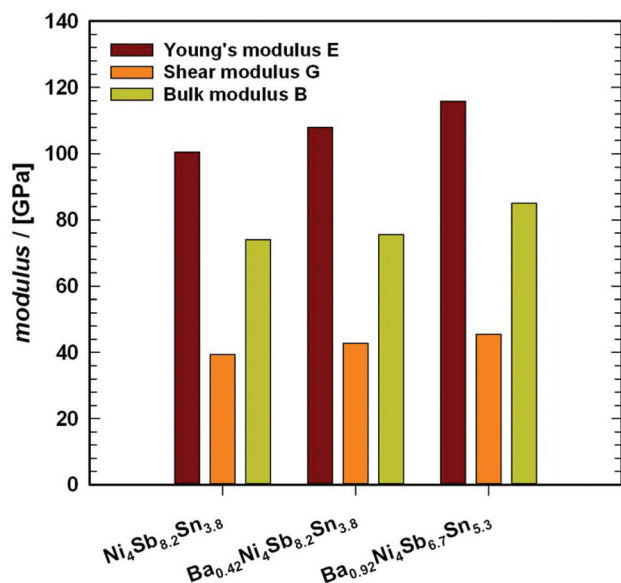
Fig. 32 Comparison of the Young's-, Shear- and Bulk-modulus obtained for the skutterudites $Ni_4Sb_{8.2}Sn_{3.8}$, $Ba_{0.42}Ni_4Sb_{8.2}Sn_{3.8}$ and $Ba_{0.92}Ni_4Sb_{6.7}Sn_{5.3}$.

11.   Vickers hardness (HV)

Hardness is a measure for a the strength of a solid, *i.e.*, the material's resistance against plastic deformation under an applied force and is dependent on ductility, elastic stiffness, plasticity, strain, strength, toughness, visco-elasticity and viscosity. This was the reason to perform the Vickers hardness test on a series of alloys, including the three single-phase bulk samples $Ni_4Sb_{8.2}Sn_{3.8}$, $Ba_{0.42}Ni_4Sb_{8.2}Sn_{3.8}$ and

$Ba_{0.92}Ni_4Sb_{6.7}Sn_{5.3}$ particularly on skutterudite crystallites above 200 nm in size. As the Vickers method is an indentation measurement, the specimen's resistance is determined against deformation due to a constant compression load from a sharp object. Fig. 33 shows the results for the skutterudites in the multiphase samples, while Fig. 34 presents data for the single-phase samples. A comparison with the data available in the literature (see for example ref. 23) shows that the HV of the $Ba_yNi_4Sb_{12-x}Sn_x$ skutterudites lay perfectly within the range of other skutterudites. From the measurements performed on the single-phase samples, two trends can be derived (Fig. 35): the hardness seems to decrease with (i) increasing Ba and Sn content and (ii) increasing Young's modulus and shear modulus. For the compounds, $Ni_4Sb_{8.49}Sn_{3.87}$, $Ba_{0.42}Ni_4Sb_{8.44}Sn_{3.88}$ and $Ba_{0.92}Ni_4Sb_{6.78}Sn_{5.41}$, the Vickers hardness after HPT processing (Fig. 34 and 35) shows no measurable change.

12.   Electron and phonon mean free path

To learn more about the transport properties caused by electrons and phonons, their mean free paths were calculated using simple models and then discussed in comparison with the resistivity and thermal conductivity data. Assuming a three-dimensional system with a spherical Fermi surface,[90] the mean free path ℓ_{el} of the electrons can be calculated from the measured resistivity data,

$$\ell_{el} = \frac{3 \cdot \pi^2 \cdot \hbar}{e^2 \cdot k_F^2 \cdot \rho(T)}. \tag{12.1}$$
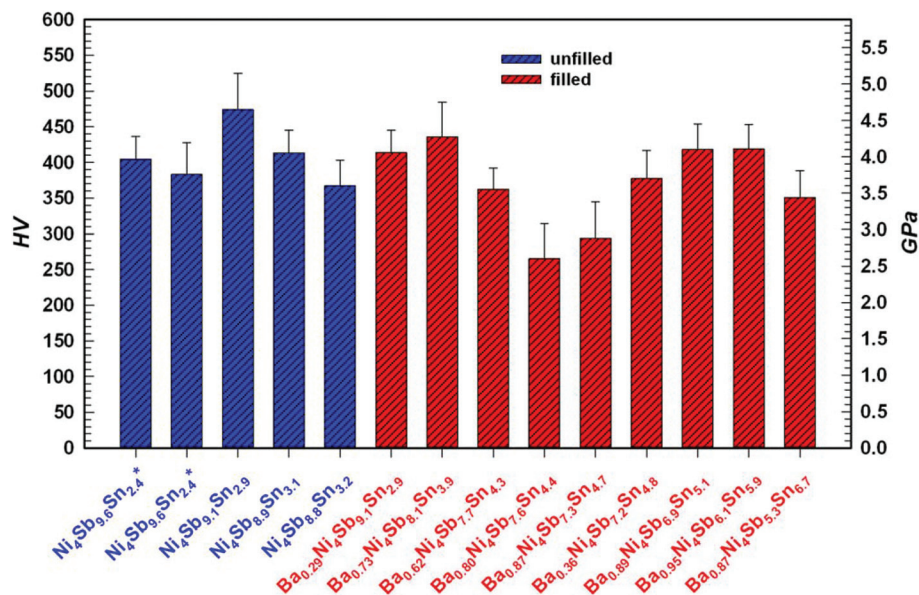

Fig. 33 Comparison of the Vicker's hardness HV for the various filled and unfilled Ni−Sn−Sb based skutterudites (* skutterudite composition in two different alloys).
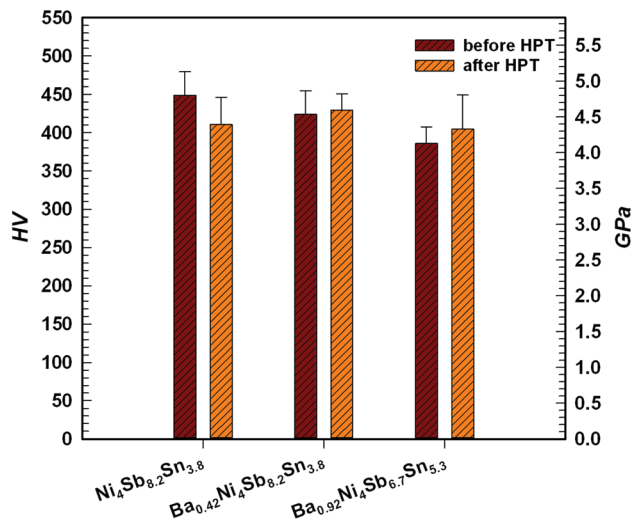
Fig. 34 Comparison of the Vicker's hardness HV for the skutterudite single-phase samples $Ni_4Sb_{8.2}Sn_{3.8}$, $Ba_{0.42}Ni_4Sb_{8.2}Sn_{3.8}$ and $Ba_{0.92}Ni_4Sb_{6.7}Sn_{5.3}$ before and after HPT.

Fig. 36 Temperature dependent electron mean free paths ℓ_{el} obtained for the skutterudites $Ni_4Sb_{8.2}Sn_{3.8}$, $Ba_{0.42}Ni_4Sb_{8.2}Sn_{3.8}$ and $Ba_{0.92}Ni_4Sb_{6.7}Sn_{5.3}$.

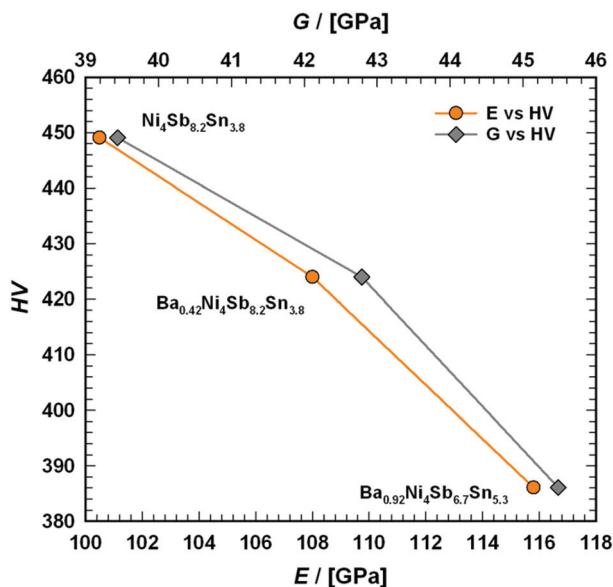**Fig. 35** Comparison of the Young's- and Shear-modulus in dependence of the Vicker's hardness HV for the skutterudites $Ni_4Sb_{8.2}Sn_{3.8}$, $Ba_{0.42}Ni_4Sb_{8.2}Sn_{3.8}$ and $Ba_{0.92}Ni_4Sb_{6.7}Sn_{5.3}$.

Herein, e is the electronic charge and $\hbar$ is the reduced Planck's constant. The Fermi wave vector k_F can be approximated by

$$k_F = \left(\frac{3}{4}\cdot\pi\right)^{\frac{1}{3}}\cdot\frac{2\cdot\pi}{a} \tag{12.2}$$

with a as the lattice parameter. Fig. 36 displays the temperature dependence of the electronic mean free path for the three single-phase samples, $Ni_4Sb_{8.2}Sn_{3.8}$, $Ba_{0.42}Ni_4Sb_{8.2}Sn_{3.8}$ and $Ba_{0.92}Ni_4Sb_{6.7}Sn_{5.3}$. For all three specimens, ℓ_{el} is five to ten

times higher than the lattice parameter a. This confirms the quite low resistivity $\rho(T)$ found in these alloys. It seems that Ba filling in the 2a site has a positive effect on ℓ_{el}, whereas increasing the Sn content in site 24g decreases ℓ_{el}.

From a simple kinetic theory, one can also estimate the phonon mean free path (eqn (12.3)), which is an important parameter for thermal conductivity:[28]

$$\kappa_{ph} = \frac{1}{3}\cdot v_g\cdot\ell_{ph}\cdot\frac{C_v}{V_m} \tag{12.3}$$

In addition to the electronic part κ_{el}, heat transport is conducted by phonons with a group velocity v_g and mean free path lengths ℓ_{ph} between the scattering processes. The amount of transported heat is also proportional to the molar heat capacity C_v. For the group velocity v_g, a common approximation takes the mean sound velocity v_m. Taking our data from elastic properties measurements, C_v can then be calculated by

$$C_v = C_p - V_m\cdot T\cdot\frac{\alpha^2}{\beta} \tag{12.4}$$

with the measured heat capacity C_p, the thermal expansion coefficient α and the molar volume V_m. β is the isothermal compressibility, with $\beta = 1/B$ and B being the bulk modulus (see our data above). As for a solid $C_p \approx C_v$, the comparison between the calculated values for C_v and the measured values for C_p (Fig. 16 and 37) confirms that eqn (12.4) holds true in the affected temperature range.

The results for the phonon mean free path lengths in the temperature range from 4 to 110 K are shown in Fig. 38. As one of the many strategies in designing high performance thermoelectric materials is to decrease κ_{ph} by increasing the

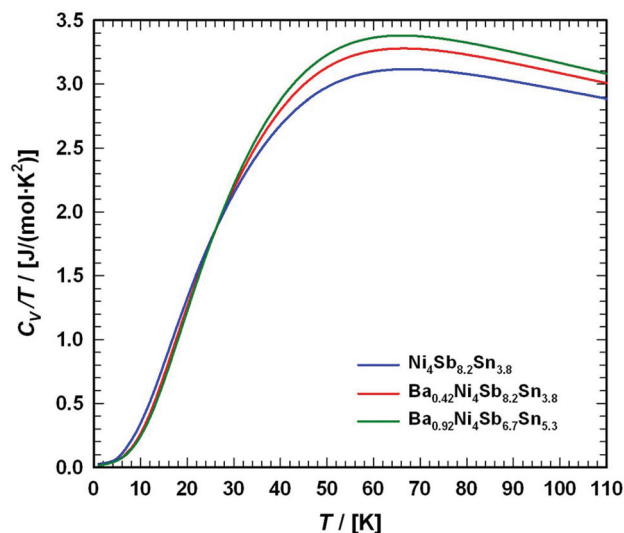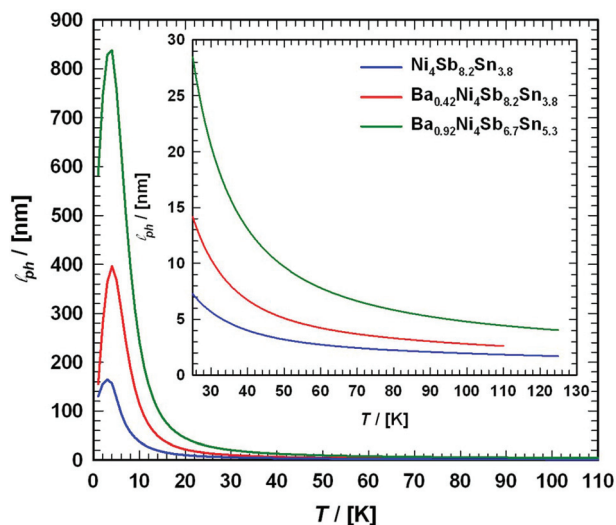Fig. 37 Temperature-dependent specific heat divided by temperature C_V/T for $Ni_4Sb_{8.2}Sn_{3.8}$, $Ba_{0.42}Ni_4Sb_{8.2}Sn_{3.8}$ and $Ba_{0.92}Ni_4Sb_{6.7}Sn_{5.3}$.

Fig. 38 Temperature dependent electron mean free paths ℓ_{ph} for the skutterudites $Ni_4Sb_{8.2}Sn_{3.8}$, $Ba_{0.42}Ni_4Sb_{8.2}Sn_{3.8}$ and $Ba_{0.92}Ni_4Sb_{6.7}Sn_{5.3}$.

phonon scattering, one can see from Fig. 38 that for $Ba_yNi_4Sb_{12-x}Sn_x$ skutterudites, this cannot be done *via* filling the 2a site with Ba as a rattling atom.

As demonstrated in various papers,[74,75] the reason for this may stem from the fact that the vibrational modes of the rattling atom are not entirely independent from the framework vibrations: the small icosahedral voids in $Ba_yNi_4Sb_{12-x}Sn_x$ squeeze the Ba-filler atoms into tight bonding (for relative cage sizes see chapter 4). It should be recalled here that reduction of the cage volume in isotypic $EuFe_4Sb_{12}$ by external pressure significantly changes the phonon structure increasing the "rattling mode" above the optical mode without avoided crossing.[91]

13. Conclusion

Phase equilibria in the ternary system Ni–Sn–Sb have been determined for the isothermal section at 450 °C, revealing a rather large extension of the $Ni_4Sn_{12-x}Sn_x$ homogeneity region from $2.4 \leq x \leq 3.2$. A combination of literature data and DTA measurements enabled us to determine the solidus surface for the unfilled $Ni_4Sn_{12-x}Sn_x$ phase as well as for the Ba-filled $Ba_yNi_4Sn_{12-x}Sn_x$ skutterudite phase. The Ba- and Sn-concentration dependent homogeneity region of the $Ba_yNi_4Sn_{12-x}Sn_x$ phase was established. Although the homogeneity region seems to extend into a p-type region, so far only n-type material was obtained.

Single-phase skutterudites samples with the composition $Ni_4Sb_{8.2}Sn_{3.8}$, $Ba_{0.42}Ni_4Sb_{8.2}Sn_{3.8}$ and $Ba_{0.92}Ni_4Sb_{6.7}Sn_{5.3}$ have been successfully prepared and characterised by their physical and mechanical properties with respect to their formation and crystal structure. Resistivity data were within a crossover from metallic to semiconducting behaviour and were successfully modeled in terms of a temperature-dependent carrier concentration in a rectangular density of states with the Fermi energy slightly below a narrow gap. The corresponding narrow gap widths – extracted from maxima in the Seebeck coefficient data as a function of temperature – are ranged about 0.050 eV. Although the resistivity $\rho(T)$ of the compounds investigated ($Ni_4Sb_{8.2}Sn_{3.8}$, $Ba_{0.42}Ni_4Sb_{8.2}Sn_{3.8}$ and $Ba_{0.92}Ni_4Sb_{6.7}Sn_{5.3}$) is quite low, the rather large thermal conductivity $\kappa(T)$ prevents the material from reaching attractive figures of merit, zT. The Debye and Einstein temperatures gathered by various methods lie within the same range and are therefore comparable to those of other skutterudites and consistent with high levels of lattice thermal conductivity. As one of the reasons for the low zT, the Ba filler atoms with rather small ADPs (atom displacement factors) at the centres of tight $Ni_4(Sb,Sn)_{12}$ cages are unable to significantly decrease the phonon mean free paths and constitute a severe reduction of the "rattling behaviour".

Severe plastic deformation (SPD) *via* high-pressure torsion (HPT) was used to introduce nanostructuring; however, the physical properties before and after HPT showed no significant effect on the materials thermoelectric behaviour.

Acknowledgements

References

1 Y. Gelbstein, Z. Dashevsky and M. P. Dariel, *Physica B*, 2007, **396**(1–2), 16–21.

2 J. Davidow and Y. Gelbstein, *J. Electron. Mater.*, 2013, **42**(7), 1542–1549.

3 K. Kirievsky, Y. Gelbstein and D. Fuks, *J. Solid State Chem.*, 2013, **203**, 247–254.

4 Y. Gelbstein, N. Tal, A. Yamek, Y. Rosenberg, M. P. Moshe, S. Ouardi, B. Balke, C. Felser and M. Kohne, *J. Mater. Res.*, 2011, **26**(15), 1919–1924.

5 Y. Sadia, L. Dinnerman and Y. Gelbstein, *J. Electron. Mater.*, 2013, **42**(7), 1926–1931.

6 C. Uher, *Thermoelectric Materials Research I*, ed. T. M. Tritt, Elsevier, 2001, pp. 139–253.

7 G. J. Snyder and E. S. Toberer, *Nat. Mater.*, 2008, **7**(2), 105–114.

8 X. Shi, J. Yang, J. R. Salvador, M. Chi, J. Y. Cho, H. Wang, S. Bai, J. Yang, W. Zhang and L. Chen, *J. Am. Chem. Soc.*, 2011, **133**(20), 7837–7846.

9 G. Rogl, A. Grytsiv, P. Rogl, N. Peranio, E. Bauer, M. Zehetbauer and O. Eibl, *Acta Mater.*, 2014, **63**, 30–43.

10 G. Rogl, A. Grytsiv, P. Rogl, E. Bauer and M. Zehetbauer, *Intermetallics*, 2001, **19**(4), 546–555.

11 G. Rogl, A. Grytsiv, P. Rogl, E. Bauer and M. Zehetbauer, *Solid State Phenomena*, 2011, **170**, 240–243.

12 M. D. Hornbostel, K. Sellinschegg and D. C. Johnson, *Thermoelectric Materials - New Directions and Approaches*, Mater. Res. Soc. Symp. Proc. Ser., Pittsburgh, 1997, vol. 478, p. 211.

13 M. D. Hornbostel, E. J. Hyer, J. Thiel and D. C. Johnson, *J. Am. Chem. Soc.*, 1997, **119**(11), 2665–2668.

14 G. S. Nolas, H. Takizawa, T. Endo, H. Sellinschegg and D. C. Johnson, *Appl. Phys. Lett.*, 2000, **77**(1), 52–54.

15 H. Takizawa, K. Miura, M. Ito, T. Suzuki and T. Endo, *J. Alloys Compd.*, 1999, **282**(1–2), 79–83.

16 H. Takizawa, M. Ito, K. Uheda and T. Endo, *J. Ceram. Soc. Jpn.*, 2000, **108**(June), 530–534.

17 H. Takizawa, K. Okazaki, K. Uheda and T. Endo, MRS Fall Meeting (Boston, MA, Nov., 2001) (abstracts), 2001, p. 123; H. Takizawa, K. Okazaki, K. Uheda and T. Endo, MRS Fall Meeting (Boston, MA, Nov. 2001) (Mater. Res. Soc. Symp. Proc. Ser. vol 691), 2002.

18 A. Grytsiv, P. Rogl, St. Berger, Ch. Paul, H. Michor, E. Bauer, G. Hilscher, R. Ferro, T. Roisnel and H. Noel, *J. Phys.: Condens. Matter*, 2002, **14**(29), 7071–7090.

19 R. Mishra, A. Kroupa, A. Zemanova and H. Ipser, *J. Electron. Mater.*, 2013, **42**(4), 646–653.

20 G. Rogl, A. Grytsiv, N. Melnychenko-Koblyuk, E. Bauer, S. Laumann and P. Rogl, *J. Phys.: Condens. Matter*, 2011, **23**(27), 275601.

21 G. Rogl, A. Grytsiv, E. Bauer, P. Rogl and M. Zehetbauer, *Intermetallics*, 2010, **18**(1), 57–64.

22 G. Rogl, L. Zhang, P. Rogl, A. Grytsiv, M. Falmbigl, D. Rajs, M. Kriegisch, H. Müller, E. Bauer, J. Koppensteiner, W. Schranz, M. Zehtbauer, Z. Henkie and B. Maple, *J. Appl. Phys.*, 2010, **107**(4), 043507.

23 G. Rogl and P. Rogl, *Sci. Adv. Mater.*, 2011, **3**(4), 517–538.

24 G. Rogl, A. Grytsiv, E. Royanian, P. Heinrich, E. Bauer, P. Rogl, M. Zehetbauer, S. Puchegger, M. Reinecker and W. Schranz, *Acta Mater.*, 2013, **61**(11), 4066–4079.

25 R. C. Mallik, R. Anbalagan, G. Rogl, E. Royanian, P. Heinrich, E. Bauer, P. Rogl and S. Suwas, *Acta Mater.*, 2013, **61**(18), 6698–6711.

26 M. Llunell, P. Alemany, S. Alvarez, V. P. Zhukov and A. Vernes, *Phys. Rev. B: Condens. Matter*, 1996, **53**(16), 10605–10609.

27 W. Jeitschko, A. J. Foecker, D. Paschke, M. V. Dewalsky, Ch. B. H. Evers, B. Kunnen, A. Lang, G. Kotzyba, U. Ch. Rodewald and M. H. Moller, *Z. Anorg. Allg. Chem.*, 2000, **626**(5), 1112–1120.

28 E. S. Toberer, A. F. May and G. J. Snyder, *Chem. Mater.*, 2010, **22**(3), 624–634.

29 K. Ishida and T. Nishizawa, *Binary Alloy Phase Diagrams*, ed. T. B. Massalski, H. Okamoto, P. R. Subramanian and L. Kacprzak, ASM International, Materials Park, Ohio, 2nd edn, 1990, vol. 1, pp. 269–270.

30 H. Okamoto, *J. Phase Equilib.*, 1991, **12**(2), 244–245.

31 W. Wacha, PhD Thesis, Vienna University of Technology, 1989.

32 J. Rodriguez-Carvajal, Satellite Mtg on Powder Diffraction of the 15th Congr. of the International Union of Crystallography (Toulouse, France) (abstracts), 1990, p. 127.

33 *Nonius Kappa CCD Program Package COLLECT, DENZO, SCALEPACK, SORTAV*, Nonius Delft, The Netherlands, 1998.

34 G. M. Sheldrick, *SHELXL-97: Program for crystal structure refinement*, University of Göttingen, Germany; Windows version OSCAIL by McArdle, Natl. Univ. Ireland, Galway; 1997.

35 E. Bauer, A. Galatanu, H. Michor, G. Hilscher, P. Rogl, P. Boulet and H. Noel, *Eur. Phys. J. B*, 2000, **14**(3), 483–493.

36 M. Rotter, H. Müller, E. Gratz, M. Dörr and M. Löwenhaupt, *Rev. Sci. Instrum.*, 1998, **69**(7), 2742–2746.

37 G. Braendii and R. Griessen, *Cryogenics*, 1973, **13**(5), 299–302.

38 J. Genossar and M. Steinitz, *Rev. Sci. Instrum.*, 1990, **61**(9), 2469–2471.

39 J. Koppensteiner, W. Schranz and M. R. Puica, *Phys. Rev. B: Condens. Matter*, 2008, **78**(5), 054203.

40 W. Schranz, *Phase Transitions*, 1997, **64**(1–2), 103–114.

41 W. Schranz and D. Havlik, *Phys. Rev. Lett.*, 1994, **73**(19), 2575–2578.

42 R. Wyslouzil, Ph.D. thesis, University of Vienna, 1985.

43 A. Migliori, J. L. Sarrao, W. M. Visscher, T. M. Bell, M. Lei, Z. Fisk and R. G. Leisure, *Physica B*, 1993, **183**(1–2), 1–24.

44 P. Scherrer, *Nachr. Ges. Wiss. Göttingen*, 1918, 96–100.

45 L. Zhang, A. Grytsiv, M. Kerber, P. Rogl, E. Bauer, M. J. Zehetbauer, J. Wonsik and G. E. Nauer, *J. Alloys Compd.*, 2009, **481**(1–2), 106–115.

46 C. Schmetterer, H. Flandorfer, K. W. Richter, U. Saeed, M. Kauffman, P. Roussel and H. Ipser, *Intermetallics*, 2007, **15**(7), 869–884.

47 G. H. Cha, S. Y. Lee and P. Nash, *Binary Alloy Phase Diagrams*, ed. T. B. Massalski, H. Okamoto, P. R. Subramanian and L. Kacprzak, ASM International, Materials Park, Ohio, 2nd edn, 1990, vol. 3, pp. 2853–2855.

48 J. Polt, Master Thesis, University of Vienna, 2014.

49 W. Burkhardt and K. Schubert, *Z. Metallkd.*, 1959, **50**, 442–452.

50 L. M. Gelato and E. Parthé, *J. Appl. Crystallogr.*, 1987, **20**, 139–143.

51 E. Koch and W. Fischer, *Z. Kristallogr.*, 1996, **211**(4), 251–253.

52 D. J. Braun and W. Jeitschko, *J. Less-Common Met.*, 1980, **72**(1), 147–156.

53 J. Lees and P. A. Flinn, *Phys. Lett.*, 1965, **19**(3), 186–188.

54 P. Gütlich, E. Bill and A. X. Trautwein, *Mössbauer Spectroscopy and Transition Metal Chemistry*, Springer, Berlin, 2011, pp. 13–15.

55 I. Devos, M. Womes, M. Heilemann, J. Olivier-Fourcade, J.-C. Jumas and J. L. Tirado, *J. Mater. Chem.*, 2004, **14**(11), 1759–1767.

56 I. Lefebvre-Devos, M. Lassalle, X. Wallart, J. Olivier-Fourcade, L. Monconduit and J. C. Jumas, *Phys. Rev. B: Condens. Matter*, 2005, **63**(12), 125110.

57 A. Junod, D. Bichsel and J. Mueller, *Helv. Phys. Acta*, 1979, **52**(5–6), 580–596.

58 A. Junod, T. Jarlborg and J. Mueller, *Phys. Rev. B: Condens. Matter*, 1983, **27**(3), 1568–1585.

59 N. Melnychenko-Koblyuk, A. Grytsiv, St. Berger, H. Kaldarar, H. Michor, F. Roehrbacher, E. Royanian, E. Bauer, P. Rogl, H. Schmid and G. Giester, *J. Phys.: Condens. Matter*, 2007, **19**(4), 046203.

60 S. M. Kauzlarich, *Encyclopedia of Inorganic chemistry*, ed. R. B. King, Wiley, New York, 2nd edn, 2005.

61 S. C. Sevov, *Zintl Phases in Intermetallic Compounds, Principles and Practice: Progress*, ed. J. H. Westbrook and R. L. Freisher, John Wiley & Sons. Ltd., Chichester, 2002, pp. 113–132.

62 St. Berger, PhD Thesis, Vienna University of Technology, 2003.

63 J. H. Chiu, *Phys. Rev. B: Solid State*, 1976, **13**(4), 1507–1514.

64 C. Hamaguchi, *Basic Semiconductor Physics*, Springer, Berlin, 2nd edn, 2010, ch. 6.

65 F. J. Blatt, *Physics of electronic conduction in solids*, McGraw-Hill, New York, 1968.

66 H. J. Goldsmid and J. W. Sharp, *J. Electron. Mater.*, 1999, **28**(7), 869–872.

67 D. W. Rowe and C. M. Bhandari, *Modern Thermoelectrics*, Reston Publishing Comp., Virginia, USA, 1983.

68 H. Wilson, *Math. Proc. Camb. Phil. Soc.*, 1937, **33**(3), 371–379.

69 J. Callaway and H. C. von Baeyer, *Phys. Rev.*, 1960, **120**, 1149–1154.

70 J. Callaway, *Phys. Rev.*, 1959, **113**, 1046–1051.

71 J. Callaway, *Phys. Rev.*, 1961, **122**, 787–790.

72 D. Cahill and R. Pohl, *Solid State Commun.*, 1989, **70**(10), 927–930.

73 K. Gianno, A. V. Sologubenko, M. A. Chernikov, H. R. Ott, I. R. Fisher and P. C. Canfield, *Phys. Rev. B: Condens. Matter*, 2000, **62**(1), 292–300.

74 M. Christensen, A. B. Abrahamsen, N. B. Christensen, F. Juranyi, N. H. Andersen, K. Lefmann, J. Andreasson, C. R. Bahl and B. B. Iversen, *Nat. Mater.*, 2008, **7**(10), 811–815.

75 M. M. Koza, M. R. Johnson, R. Viennois, H. Mutka, L. Girard and D. Ravot, *Nat. Mater.*, 2008, **7**(10), 805–810.

76 G. Rogl, M. Zehetbauer, M. Kerber, P. Rogl and E. Bauer, *Mater. Sci. Forum*, 2011, **667–669**, 1089–1094.

77 G. Rogl, D. Setman, E. Schafler, J. Horky, M. Kerber, M. Zehetbauer, M. Falmbigl, P. Rogl, E. Royanian and E. Bauer, *Acta Mater.*, 2012, **60**(5), 2146–2157.

78 G. Rogl, Z. Aabdin, E. Schafler, J. Horky, D. Setman, M. Zehetbauer, M. Kriegisch, O. Eibl, A. Grytsiv, E. Bauer, *et al.*, *J. Alloys Compd.*, 2012, **537**, 183–189.

79 L. D. Hicks, T. C. Harman and T. C. Dresselhaus, *Appl. Phys. Lett.*, 1993, **63**(23), 3230–3232.

80 M. S. Dresselhaus and J. P. Heremans, *Thermoelectrics handbook*, Wiley, New York, 2003, p. 1338.

81 M. J. Zehetbauer and Y. Estrin, *Bulk nanostructured materials*, ed. M. J. Zehetbauer and Y. T. Zhu, VCH Wiley, New York, 2009.

82 L. Zhang, A. Grytsiv, B. Bonarski, M. Kerber, D. Setman, E. Schafler, P. Rogl, E. Bauer, G. Hirschler and M. Zehetbauer, *J. Alloys Compd.*, 2010, **494**(1–2), 78–83.

83 E. Schafler, A. Dubravina, B. Mingler, H. P. Karnthaler and M. Zehetbauer, *Mater. Sci. Forum*, 2006, **503–504**, 57–64. See also: G. M. Sheldrick, *Acta Crystallogr., Sect. A: Fundam. Crystallogr.*, 2008, **64**(Pt 1), 112–122.

84 T. Ungar and M. Zehetbauer, *Scr. Mater.*, 1996, **35**(12), 1467–1473.

85 M. Zehetbauer and V. Seumer, *Acta Metall. Mater.*, 1993, **41**(2), 577–588.

86 M. Zehetbauer, H. P. Stuwe, A. Vorauer, E. Schafler and J. Kohout, *Adv. Eng. Mater.*, 2003, **5**(5), 330–337.

87 M. Zehetbauer, E. Schafler, G. Steiner and A. Korznikova, *Mater. Sci. Forum*, 2006, **503–504**, 57–64.

88 G. D. Mukherjee, C. Bansal and A. Chatterjee, *Phys. Rev. Lett.*, 1996, **76**(11), 1876–1879.

89 O. L. Anderson, *J. Phys. Chem. Solids*, 1963, **24**, 909–917.

90 O. Gunnarsson, M. Calandra and J. E. Han, *Rev. Mod. Phys.*, 2003, **75**(4), 1085–1099.

91 I. Sergueev, K. Glazyrin, I. Kantor, M. A. McGuire, A. I. Chumakov, B. Klobes, B. C. Sales and R. P. Hermann, *Phys. Rev. B: Condens. Matter*, 2015, **91**(22), 1–7.